Arctic sea level variability from high-resolution model simulations and implications for the Arctic observing system

Guokun Lyu[1,2], Nuno Serra[2], Meng Zhou[1], and Detlef Stammer[2]

[1] School of Oceanography, Shanghai Jiao Tong University, Shanghai, 200030, China

[2] Center for Earth System Research and Sustainability (CEN), University of Hamburg, Hamburg, 20146, Germany

Correspondence to: Guokun Lyu (guokun.lyu@sjtu.edu.cn)

8   **Abstract.** Two high-resolution model simulations are used to investigate the spatio-temporal variability of the

9   Arctic Ocean sea level. The model simulations reveal barotropic sea level variability at periods <30 days, which

10   is strongly captured by bottom pressure observations. The seasonal sea level variability is driven by volume

11   exchanges with the Pacific and Atlantic Oceans and the redistribution of the water by the wind. Halosteric ef-

12   fects due to river runoff and evaporation minus precipitation (EmPmR), ice melting/formation also contribute in

13   the marginal seas and seasonal sea ice extent regions. In the central Arctic Ocean, especially the Canadian Basin,

14   the decadal halosteric effect dominates sea level variability. The study confirms that satellite altimetric observa-

15   tions and Gravity Recovery and Climate Experiment (GRACE) could infer the total freshwater content changes

16   in the Canadian Basin at periods longer than one year, but they are unable to depict the seasonal and subseasonal

17   freshwater content changes. The increasing number of profiles seems to capture freshwater content changes

18   since 2007, encouraging further data synthesis work with a more complicated interpolation method. Further, in-

19   situ hydrographic observations should be enhanced to reveal the freshwater budget and close the gaps between

20   satellite altimetry and GRACE, especially in the marginal seas.

1 Introduction

The Arctic Ocean is experiencing pronounced changes (e.g., Perovich et al., 2020; AMAP, 2019). Observations have revealed increased warm inflows through the Bering Strait (Woodgate et al., 2012) and the Fram Strait (Polyakov et al., 2017), and an unprecedented freshening of the Canadian Basin, especially the Beaufort Gyre (Proshutinsky et al., 2019). The rapid changes potentially impact the weather and climate of the northern hemisphere (Overland et al., 2021).

As an integrated indicator, sea level change reflects changing ocean conditions caused by ocean dynamics, atmospheric forcing, and terrestrial processes (Stammer et al., 2013). Satellite altimetry, together with bottom pressure observations from Gravity Recovery and Climate Experiment (GRACE), has been applied to infer ocean temperature and salinity changes that are not measured directly in the Arctic Ocean (e.g., Armitage et al., 2016) and in the deep ocean (e.g., Llovel et al., 2014), enhancing our ability to monitor ocean changes.

Over the past decades, coupled ocean-sea ice models and observations have advanced our understanding of the Arctic Ocean variability. Proshutinsky and Johnson (1997) demonstrated wind-forced cyclonic/anticyclonic ocean circulation patterns accompanied by dome-shaped sea levels variation using a barotropic model simulation. Further, ocean circulation changes in the Canadian Basin result in freshwater accumulation and release, which is very well correlated to sea level changes (Koldunov et al., 2014;Proshutinsky et al., 2002). Given that sea level changes reflect freshwater content changes in the Canadian Basin, Giles et al. (2012) and Morison et al. (2012) proposed to use satellite altimetry observations and GRACE observations to infer freshwater content changes. The method was then applied to explore the freshwater content changes in the Beaufort Gyre (Armitage et al., 2016;Proshutinsky et al., 2019) at seasonal to decadal timescales. In the Barents Sea, Volkov et al. (2013) used altimetric sea level observations and the ECCO reanalysis (Forget et al., 2015) to explore seasonal to interannual sea level anomalies, revealing different roles of mass-related changes, thermosteric and halosteric effects on different regions of the Barents Sea.

However, the sparseness of in-situ profiles, coarse resolution and significant uncertainties of satellite altimetry and GRACE observations result in large gaps in understanding the spatio-temporal variability of the Arctic sea level and its relations to the thermo/halosteric effects and mass changes (Ludwigsen and Andersen, 2021). Previous studies mainly focus on the decadal sea level variability (e.g., Koldunov et al., 2014;Proshutinsky et al., 2007;Proshutinsky and Johnson, 1997), and no study has yet fully explored the Arctic sea level variability at different spectral bands, and its dependence on the mass component and the vertical oceanic variability. Such a study could help identify critical regions and environmental parameters that need to be observed coordinately and point out observational gaps that need to be filled in the future.

Our study systematically explores the Arctic sea level variability as a function of timescale and geographic location using daily and monthly outputs of two high-resolution model simulations. Contributions from barotropic changes expressed in bottom pressure variations and baroclinic processes represented by thermo/halosteric changes are quantified at different timescales. Altimetric and GRACE measurements, in-situ hydrographic observations mapped with different interpolation schemes (e.g., Haine et al., 2015;Polyakov et al., 2008;Rabe et al., 2014;Rabe et al., 2011), and ocean reanalyses have been used to infer the basin-scale freshwater changes during the unprecedented freshwater changes since the 2000s. However, Solomon et al. (2021) pointed out that significant uncertainties and discrepancies remain in revealing the regional patterns. This study further discusses the existing Arctic observing system's capability to monitor the Arctic freshwater content

61 variability and identify observational gaps.

62   The structure of the remaining paper is as follows: the numerical models and the observations from the bot-
63 tom pressure sensor, GRACE, and satellite altimetry are described in Section 2, together with different compo-
64 nents of sea level changes. We compare the model simulations against observations in Section 3. Section 4 ana-
65 lyzes sea level variability and associated mechanisms at high frequency (<30 days), seasonal cycles, and decadal
66 timescales. The relations with bottom pressure and thermos/halosteric components are demonstrated, pointing
67 out key regions and parameters we need to observe. Further, we analyze the ability of satellite altimetry,
68 GRACE, and the in-situ profiler system to monitor the Arctic freshwater content variability in Section 5. Sec-
69 tion 6 provides a summary and conclusions.

70 **2 Model Simulations and observations**

71 **2.1 Atlantic-Arctic simulations**

72   This study relies on two ocean high-resolution numerical simulations using the MIT general circulation
73 model (Marshall et al., 1997). A dynamic thermodynamic sea ice model (Hibler, 1979, 1980;Zhang and
74 Rothrock, 2000), implemented by Losch et al. (2010), is employed to simulate sea ice processes. The model
75 domain covers the entire Arctic Ocean north of the Bering Strait and the Atlantic Ocean north of 33°S. In the
76 horizontal, the model uses a curvilinear grid with resolutions of ~8 km (ATLARC08km) and ~4 km (AT-
77 LARC04km). In the vertical, ATLARC08km has 50 levels with resolution ranging from 10 m over the top 130
78 m to 456.5 m in the deep basin. And ATLARC04km has 100 z-levels ranging from 5 m over the top 200 m to
79 185 m in the deep basin.

80   At the ocean surface, the model simulations are forced by momentum, heat, and freshwater fluxes comput-
81 ed using bulk formulae and either the 6-hourly NCEP RA1 reanalysis (Kalnay et al., 1996) (ATLARC08km) or
82 the 6-hourly ECMWF ERA-Interim reanalysis (Dee et al., 2011) (ATLARC04km). A virtual salt flux parame-
83 terization is used to mimic the dilution and salinification effects of rainfall, evaporation, and river discharge.
84 The models are forced by the monthly output from the GECCO2 (Köhl, 2015) global model configuration at the
85 open boundaries. The river runoff is applied at river mouths by seasonal climatology (Fekete et al., 2002). Bot-
86 tom topography is derived from the ETOPO 2-min (Smith and Sandwell, 1997) database. ATLARC08km is
87 initialized with annual mean temperature and salinity from the World Ocean Atlas 2005 (Boyer et al., 2005) and
88 covers 1948 to 2016, and ATLARC04km starts from the initial condition, including velocity, temperature, and
89 salinity, of ATLARC08km at the start of the year 2002. Table 1 summarizes both the simulations and their main
90 characteristics.

91 Table 1. Summary of model simulations used in this study.

	Horizontal resolution	Vertical grid	Surface forcing	periods	Output Frequency	Variables used
ATLARC08km	~8 km	50 z-levels	NCEP-RA1	1948-2016	monthly	Potential temperature
				05.01.2003-	daily	Salinity
				01.12.2010		Sea surface height

ATLARC04km	~4 km	100 z-levels	ERA-Interim	01.01.2003- 23.08.2012	daily	Wind stress

92

2.2 Satellite and in-situ observations

Koldunov et al. (2014) have validated ATLARC08km against tide gauge observations. We further compare the two model simulations against in-situ bottom pressure observations, GRACE observations, and satellite altimetric observations.

The monthly altimetric sea level observations from Armitage et al. (2016, http://www.cpom.ucl.ac.uk/dynamic_topography/) and GRACE measurements (Chambers and Bonin, 2012, doi:10.5067/TEOCN-3AJ64) are used in comparison with the model simulations. For the very high-frequency variability, bottom pressure records supplied by the Beaufort Gyre Exploration Project (BGEP, M_a, M_b, M_c, and M_d in Fig. 1, https://www2.whoi.edu/site/beaufortgyre/data/mooring-data/) and the North Pole Environmental Observatory (NPEO, M_{npeo} in Fig.1, ftp://northpoleftp.apl.washington.edu/NPEO_Data_Archive/) are used. Tidal signals are removed using the T_TIDE Matlab program (Pawlowicz et al., 2002) since the model did not include tidal forcing.

105
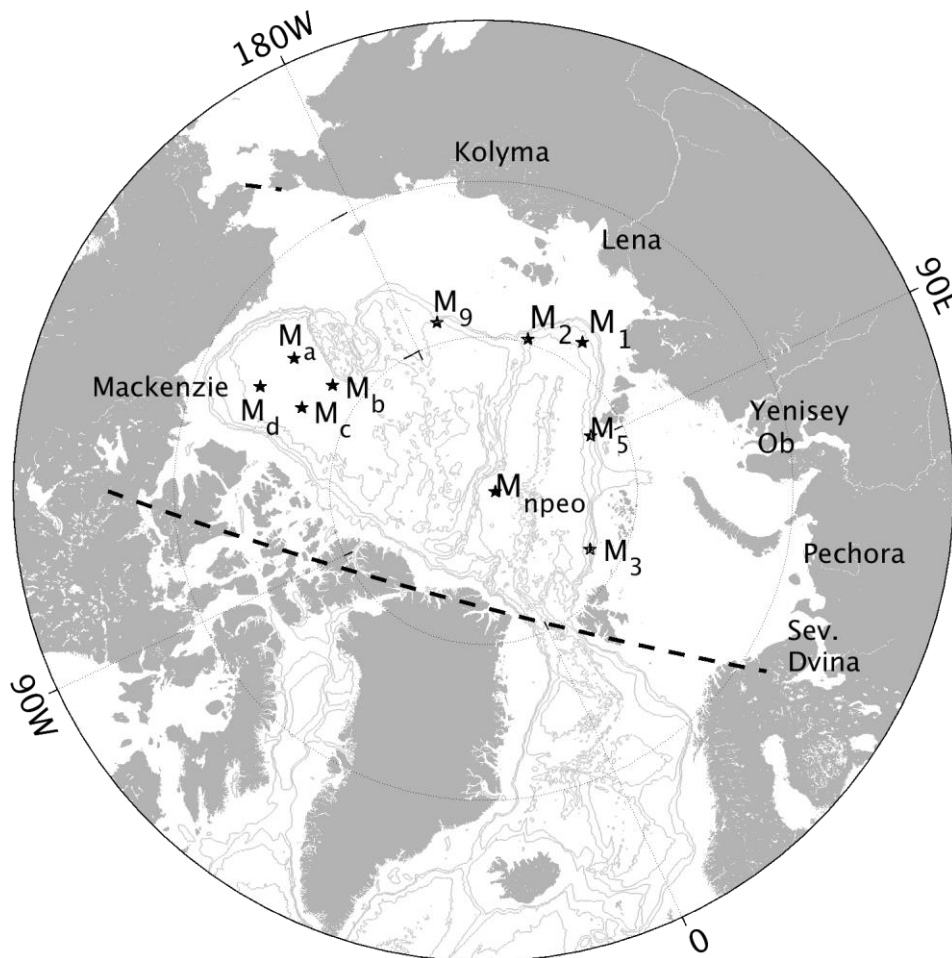
Figure 1. A map of the pan-Arctic Ocean presenting the locations of moorings deployed by the Nansen and Amundsen Basin Observational System (NABOS, black pentagrams labeled with M_1, M_2, M_3, M_5, and M_9), by the Beaufort Gyre Exploration Project (BGEP, black pentagrams marked with M_a, M_b, M_c, M_d), and by the

109 North Pole Environmental Observatory (NPEO, black pentagram labeled with M_{npeo}). The black dashed lines
110 enclose the Arctic regions used in the following sections. Bathymetry contours of 500, 1000, 2000, 3000, and
111 4000 m are drawn with grey lines. Main rivers are labeled with their names near the river mouths.

112 **2.3 Relation between sea level, bottom pressure, and thermo/halosteric components**

113   Following Ponte (1999) and Calafat et al. (2013), sea level anomaly η', can be separated into a steric com-

114 ponent η'_s due to density change, an inverse barometer effect η'_{IB}, and a mass (measured by bottom pressure

115 observations) component η'_m:

116 $\qquad \eta' = -\frac{1}{\rho_0}\int_{-H}^{0}\rho' dz + \frac{1}{\rho_0 g}(\bar{P'_a} - P'_a) + \frac{1}{\rho_0 g}(P'_b - \bar{P'_a})$ (1)

117 where g=9.8 m s^{-2} is the gravitational acceleration. The first term on the right-hand side represents the steric

118 effect η'_s, with ρ_0 being a reference density (1025.0 kg/m^3 in this study) and ρ' being the density change. The

119 second term is the inverse barometer effect η'_{IB}: $\bar{P'_a}$ and P'_a represent air pressure anomalies average over the

120 global ocean and at the observing location, respectively. The last term defines the mass component η'_m. P'_b is the

121 bottom pressure anomalies in equivalent meters of water.

122   Since the model simulations do not include the impacts of surface air pressure anomalies, the model-

123 simulated sea level changes due to steric and mass components are simplified as:

124 $\qquad \eta' = -\frac{1}{\rho_0}\int_{-H}^{0}\rho' dz + \frac{1}{\rho_0 g}(P'_b)$ (2).

125   Separating density changes into temperature and salinity changes, we decompose the steric height η'_s into

126 thermosteric height η'_{st} (due to temperature anomalies) and halosteric height η'_{ss} (due to salinity anomalies):

127 $\qquad \eta'_{st} = -\frac{1}{\rho_0}\int_{-H}^{0}\left(\rho(T,\bar{S},p) - \rho(\bar{T},\bar{S},p)\right)dz$ (3),

128 $\qquad \eta'_{ss} = -\frac{1}{\rho_0}\int_{-H}^{0}\left(\rho(\bar{T},S,p) - \rho(\bar{T},\bar{S},p)\right)dz$ (4),

129 where *T*, *S*, and *p* represent seawater temperature, salinity, and pressure. The overbars denote the average over

130 the simulation time.

131   Before comparing the model simulation with the GRACE measurements and mooring-based bottom pres-

132 sure observations, we remove air pressure anomalies averaged over the global ocean $\bar{P'_a}$, and then global-mean

133 mass changes from GRACE-based bottom pressure observations since the virtual salt flux parameterization does

134 not include mass transfer from land to ocean. In total, this process removes a seasonal cycle with an amplitude

135 of ~1-1.5 cm from the measurements.

136 **3 Testing simulations against observations**

137   Koldunov et al. (2014) have demonstrated that the interannual sea level variability in ATLARC08km and

138 tide gauges match very well. In the present study, we further evaluate the skill of the model-simulated sea level

139 and bottom pressure variability by comparing the root mean square (RMS) variability of sea level and bottom

140 pressure against altimetric data (Armitage et al., 2016) and GRACE data (Chambers and Willis, 2010). In addi-

141 tion, high-frequency bottom pressure observations from BGEP and NPEO are compared with the two model

142 simulations.
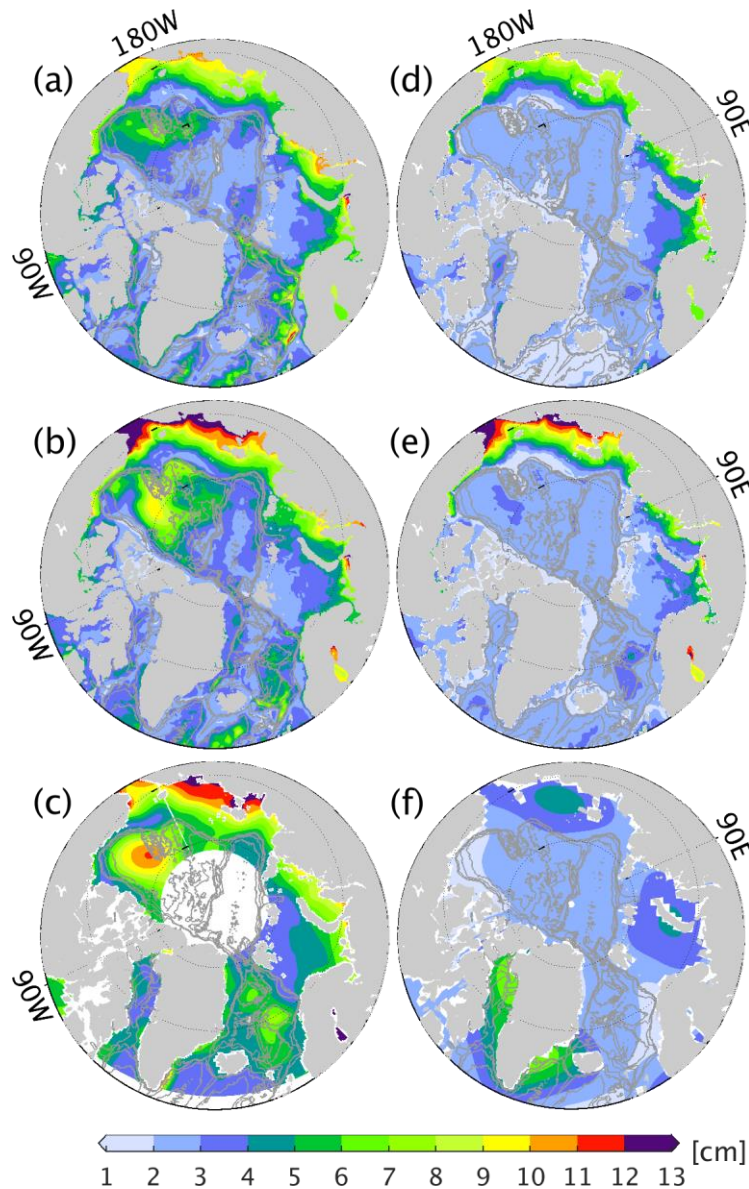
Figure 2. RMS variability of (a-c) sea level and (d-f) bottom pressure in (a, d) ATLARC08km, (b, e) ATLARC04km, (c) satellite altimetry, and (f) GRACE. We computed the RMS variability using monthly data from January 2003 to December 2011. Bathymetry contours of 500, 1000, 2000, and 3000 m are drawn with grey lines.

The model simulations (Figs. 2a, b) and satellite altimetry (Fig. 2c) reveal pronounced sea level variability in the Canadian Basin and along the coast. In the Canadian Basin, where a characteristic scale of the Rossby radius is ~10–15 km (Nurser and Bacon, 2014), ATLARC04km starts to resolve transient eddies and thereby simulates more significant sea level variability than ATLARC08km, and matches better with the observed sea level variability. Still, ATLARC04km and ATLARC08km underestimate the observed sea level variability in the Candian Basin. Along the Arctic coast, the pronounced sea level variability is related to the seasonal river runoff, the redistribution of water due to the shifting of basin-scale cyclonic/anticyclonic wind (Proshutinsky and Johnson, 1997). Again, ATLARC04km simulates much stronger sea level variability than ATLARC08km and is comparable to the altimetric observations. Bottom pressure shows significant variability in the Arctic marginal seas (Figs. 2d-f), especially in the East Siberian Sea. However, due to the smoothing process applied on GRACE measurements (a 500 km Gaussian filter), both the model simulations simulate much stronger RMS

158 variability of bottom pressure. The coarse GRACE resolution, uncertainties in the altimetric measurements, and
159 a lack of in-situ hydrographic observations results in gaps in closing the budget of sea level trend and changes,
160 especially in the Kara, Laptev, and the East Siberian seas (Ludwigsen and Andersen, 2021) where in-situ hydro-
161 graphic data are rare and altimetric measurements are less correlated with tide gauge data (Armitage et al.,
162 2016).

163
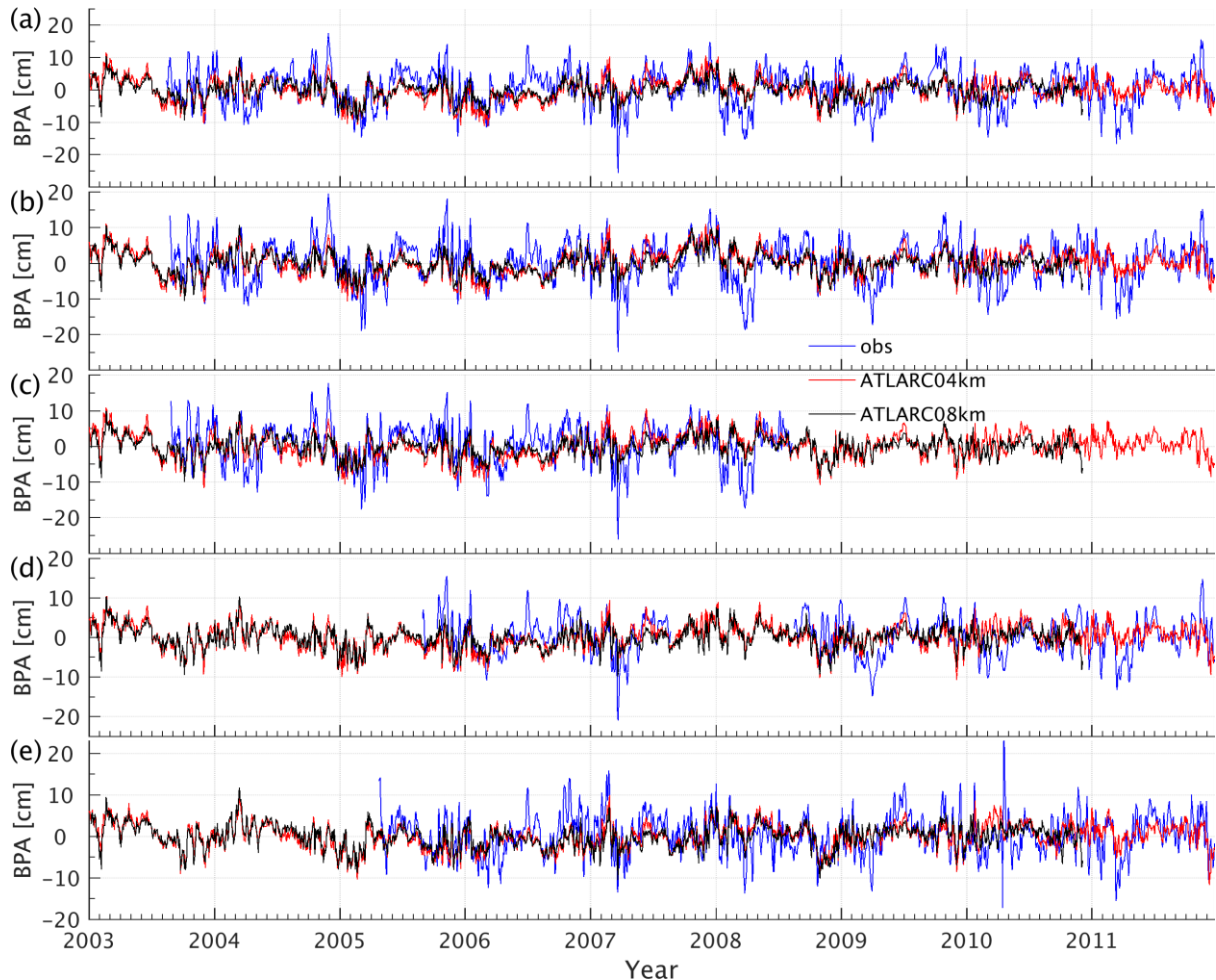
164

165 Figure 3. Time series of bottom pressure anomalies in ATLARC08km, ATLARC04km, and in-situ observations.
166 Observations are derived from (a) mooring A, (b) mooring B, (c) mooring C, and (d) mooring D of BGEP. Pan-
167 el (e) is from the NEPO moorings. Mooring locations are marked in Fig. 1.

168 Besides monthly to decadal variability of bottom pressure, both the model simulations and the in-situ ob-
169 servations also demonstrate significant high-frequency bottom pressure anomalies (Fig. 3). Both model simula-
170 tions correlate well with the observations (~0.45-0.55) in the five shown locations, but ATLARC04km and
171 ATLARC08km underestimate the RMS variability by ~30-50%, with ATLARC04km showing relatively
172 stronger RMS variability.

173 The comparisons above indicate that the model simulations reasonably reproduce the observed sea level
174 and bottom pressure variability at both high-frequency and low-frequency bands. In the following parts, we will
175 use the daily output of ATLARC04km to reveal spatial variability of sea level at high frequency and seasonal
176 periods and use the monthly output of ATLARC08km to explore the decadal sea level variability.

4 Sea level variability and its relation with bottom pressure and steric height

A model study (Proshutinsky et al., 2007) and satellite observations (Armitage et al., 2016) showed that the Arctic sea level presents distinctive seasonal to decadal variability. In situ bottom pressure observations also reveal energetic variability at sub-monthly frequencies. Here, we concentrate on sea level variability at very high-frequency (<30 days), on the seasonal cycle, and at decadal timescales (>4 years).
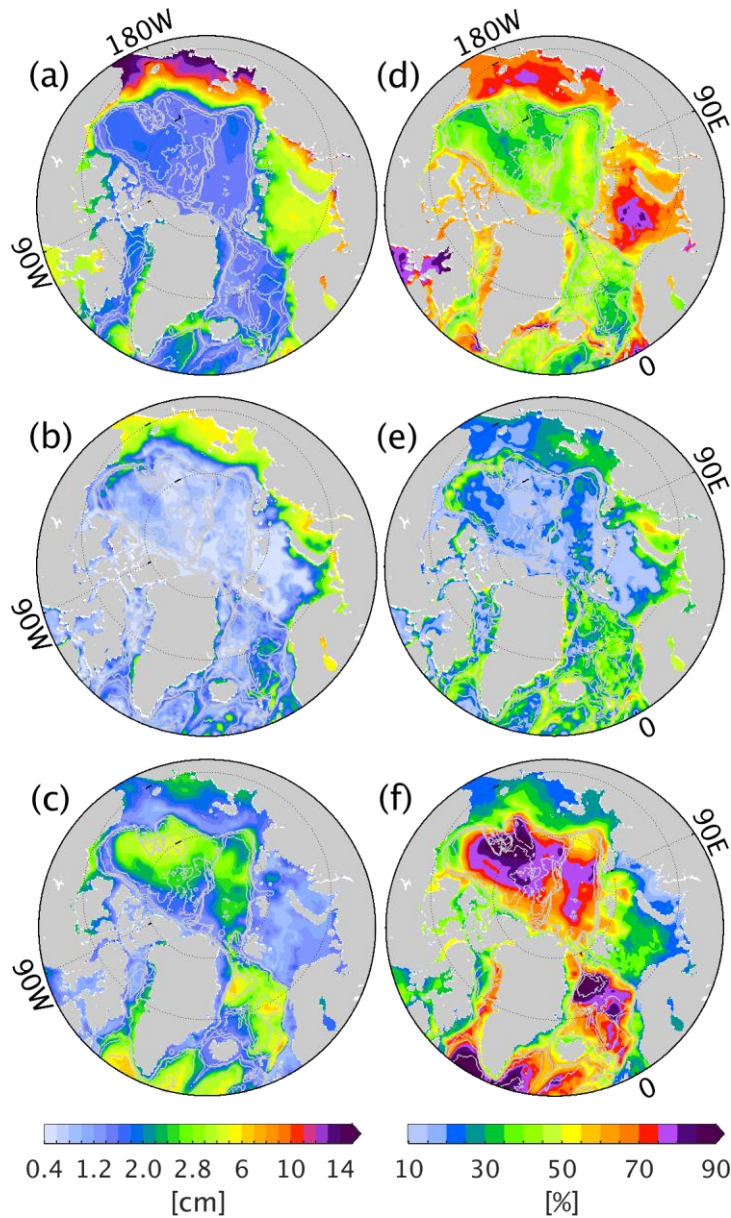
Figure 4. RMS variability (cm) of sea level (a) in the high-frequency band (<30 days), (b) at the seasonal cycle, and (c) at decadal periods (>4 years). Panels (d)-(f) are the corresponding ratios (%) to the total sea level variance that panels (a)-(c) explained. The high-frequency and seasonal variability (a, b, d, and e) uses the daily output of ATLARC04km, and decadal variability (c and f) uses the monthly output from ATLARC08km. The grey lines denote bathymetry contours of 500, 1000, 2000, and 3000 m.

At period <30 days, RMS variability of sea level up to 14 cm appears in the marginal seas and along the coasts (Fig. 4a), accounting for 60%~80% of the local sea level variance (Fig. 4d). The seasonal sea level varia-

bility is pronounced in the marginal seas and southern edge of the Beaufort Sea, and it explains 20%-40% of the total sea level variance. In the deep regions of the pan-Arctic Ocean, the decadal variability dominates the sea level variability, and it explains more than 70%~90% of the sea level variability. Overall, in the marginal seas, sea level variability is dominated by sub-monthly and seasonal signals. In contrast, decadal sea level variability dominates in the deep regions of the pan-Arctic Ocean. Besides, seasonal variability is also visible in the southern periphery of the Beaufort Sea, indicating possible exchanges between the marginal seas and the Beaufort Sea.

4.1 High-frequency (<30 days) variability

With a coarse resolution model simulation, Vinogradova et al. (2007) demonstrated that sea level variability is coherent with and virtually equivalent to bottom pressure in the mid-latitude and subpolar regions at periods <100 days, reflecting the barotropic nature of high-frequency variability (Stammer et al., 2000). Here, we revisit the high-frequency sea level variability in the pan-Arctic Ocean with high-resolution model simulations and a transfer function (Vinogradova et al., 2007) of sea level and bottom pressure.
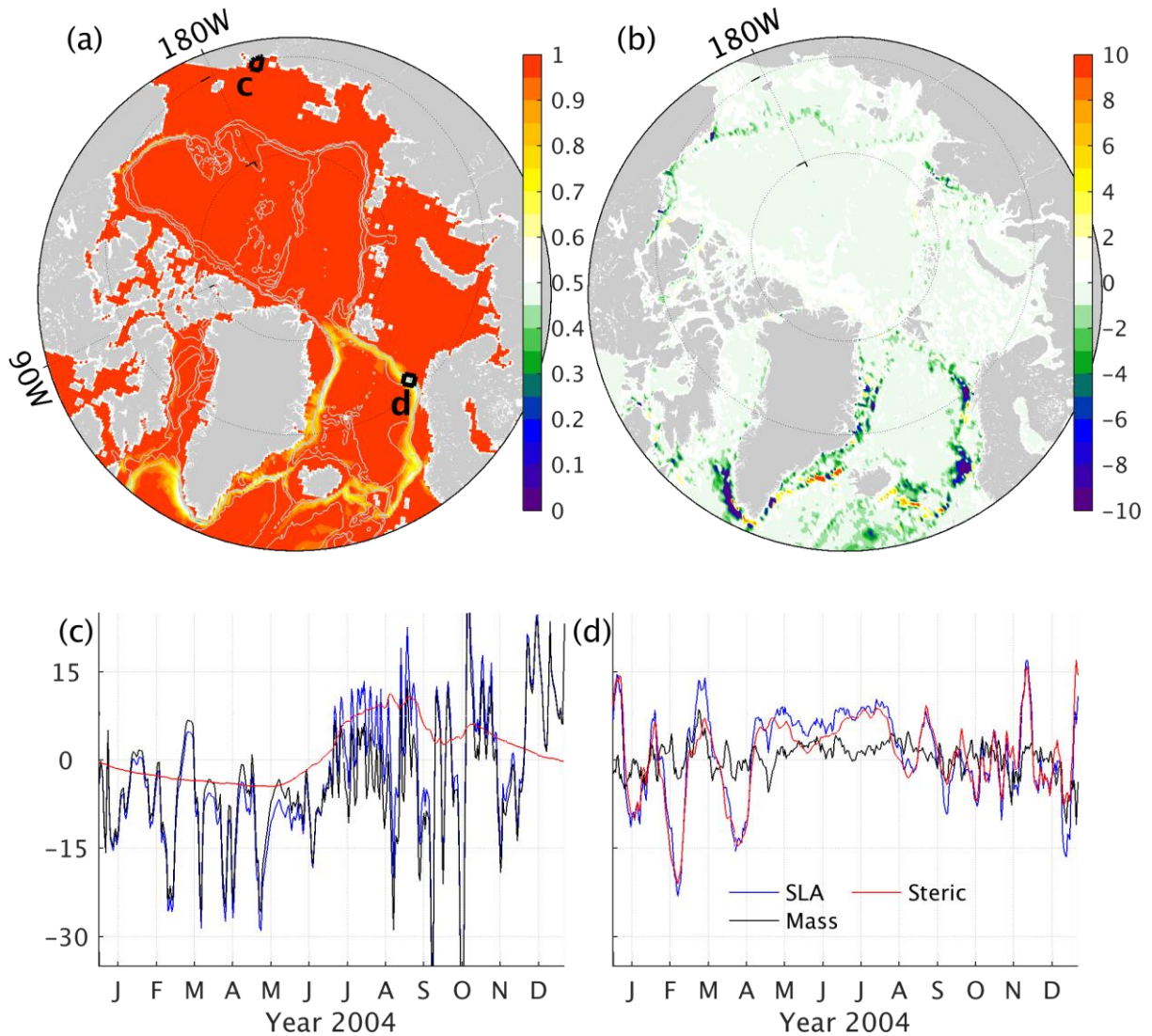
Figure 5. (a) Amplitude and (b) phase of the transfer function between sea level anomaly and bottom pressure anomaly at periods <30 days. Time series of sea level anomaly (blue lines), mass component (black lines), and steric component (red lines) averaged (c) in the East Siberian Sea (black box c in panel (a)) and (d) along the NwAC (black box d in panel (a)).

Except for the Norwegian Atlantic Current (NwAC) and the East/West Greenland Current (EGC/WGC), the amplitude of the transfer function between sea level and mass component is ~1 (Fig. 5a) in most of the pan-Arctic regions. The phases (Fig. 5b) are ~0 in the entire Arctic Ocean, indicating that the high-frequency sea level variability is mostly barotropic. However, in the strong current regions, including NwAC, EGC, and WGC, an amplitude of the transfer function of ~0.4 is observed, revealing that both barotropic and baroclinic processes contribute to the high-frequency sea level variability.

Sub-regions in the East Siberian Sea (c in Fig. 5a) near the maximum RMS variability and along the NwAC (d in Fig. 5a) are used to reveal details of the high-frequency sea level variability. It is clear that the sea level anomaly in the East Siberian Sea (Fig. 5c) is almost equivalent to the bottom pressure anomaly, and the steric component contributes slightly to the seasonal timescale. Along the NwAC (Fig. 5d), pronounced steric height variability with timescales of 20-60 days is visible, which may be caused by baroclinic instability, and the mass component shows high-frequency variability.

The high-frequency sea level variability is mainly related to wind forcing (Fukumori et al., 1998) at high latitudes. Correlations to the wind forcing and sea level anomalies are used to explain the driving mechanisms of the high-frequency SLA variability. The negative correlations between high-frequency sea level variability and wind stress curl (shading in Fig. 6a) in the Canadian Basin and GIN seas (-0.3) and in the marginal seas (-0.3~-0.5) reveal that local sea level increase/decrease is partially related to wind-induced convergence/divergence (vectors and shading in Fig. 6a) of water. In addition, the high correlations of SLA to wind stress (vectors in Fig. 6a) along the coast reveal that cyclonic along-shore wind distributes water to the coast through Ekman transport, increasing sea level there.

To further explore the propagating features of the strong SLA variability along the coasts, we show correlations of SLA in sub-regions of the East Siberian Sea (blue pentagon Fig. 6b) and Norwegian coast (blue pentagon Fig. 6c) to SLA (shading), and wind stress (vectors). Fig. 6b demonstrates that anticyclonic wind stress distributes water to the coast through Ekman transport which interacts with topography, rising coastal sea levels. SLA in the Norwegian coast is also driven by along-shore wind (vectors in Fig. 6c) through Ekman transport, and the SLA signals propagate along the coast to the Barents Sea and the central Arctic Ocean (shading in Fig. 6c).
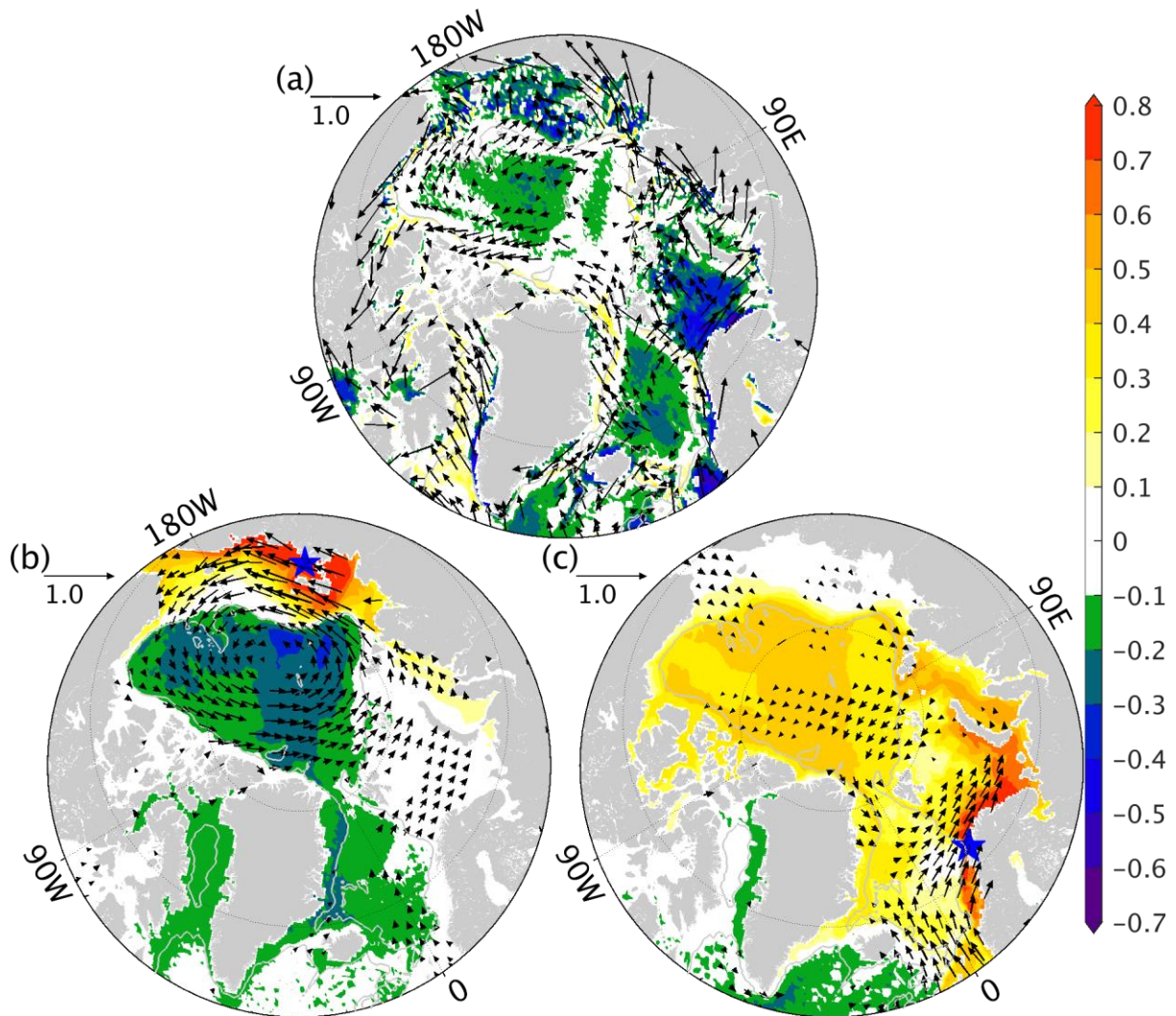
Figure 6. (a) Coefficients of the correlation between sea level anomalies and wind stress curl (shading), wind stress (vectors) at periods <30 days. (b) Correlations of sea level anomalies in sub-regions of the East Siberian Sea (blue pentagram in panel (b)) to wind stress (vectors) and sea level anomalies (shading). Panel (c) are the same as panel (b) but for sea level anomalies in the Norwegian shelf (blue pentagram in panel (c)). Correlation coefficients with 95% significance levels are plotted.

Overall, both the model simulations and the several bottom pressure records demonstrate high-frequency bottom pressure variability in the Arctic Ocean (Fig. 3). The model simulations reveal that the high-frequency variability is barotropic primarily in response to wind-induced Ekman transport and propagations of the barotropic signals. In the strong current regions, steric effects also contribute to local sea level variability caused by baroclinic processes.

4.2 Seasonal variability

Seasonal sea level variability could be related to the redistribution of water from the deep ocean to the marginal seas due to cyclonic/anticyclonic wind stress (Proshutinsky and Johnson, 1997), a seasonal variation of the Arctic Ocean volume (Armitage et al., 2016). In addition, the steric effect due to warm Atlantic inflow and

251 sea ice formation/melting contribute to regional sea level variability in the Barents Sea (Volkov and Landerer,
252 2013). This section focuses on the spatial-varying Arctic sea level variability at seasonal periods and its mecha-
253 nism.
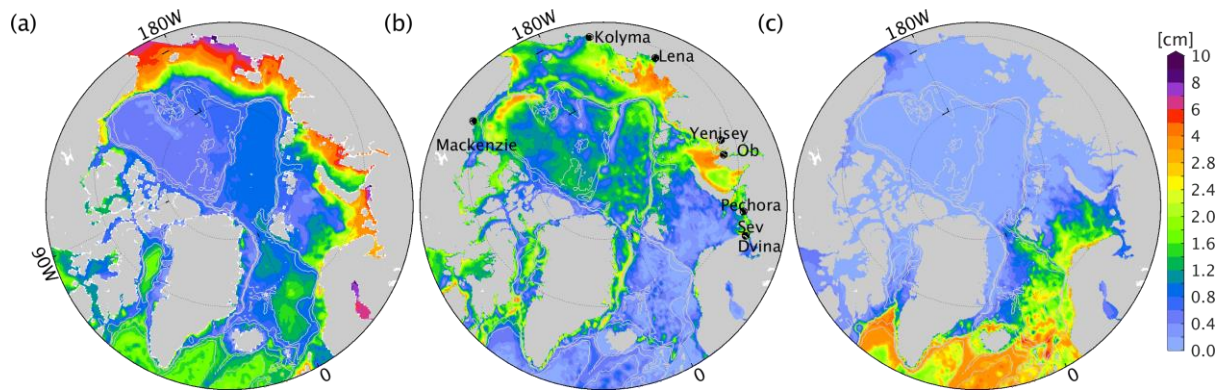
255 Figure 7. RMS variability of (a) mass, (b) halosteric, and (c) thermosteric components at the seasonal periods.

256   Like the high-frequency sea level variability, the mass component still dominates the seasonal sea level
257 variability in the marginal seas (Fig. 4b and Fig. 7a). Halosteric effects are significant near the river mouth,
258 seasonal ice edge, and along the coast of Alaska (Fig. 7b), indicating the spreading of freshwater driven by oce-
259 anic flows. Pathways of freshwater from rivers and marginal seas to the Makarov Basin and the periphery of the
260 Beaufort Sea can also be inferred from the significant halosteric effect. The thermosteric effects dominate the
261 ice-free region in the GIN seas and the Barents Sea, and it is remarkably weakened as it penetrates the ice-
262 covered Arctic Ocean (Fig. 7c).

263
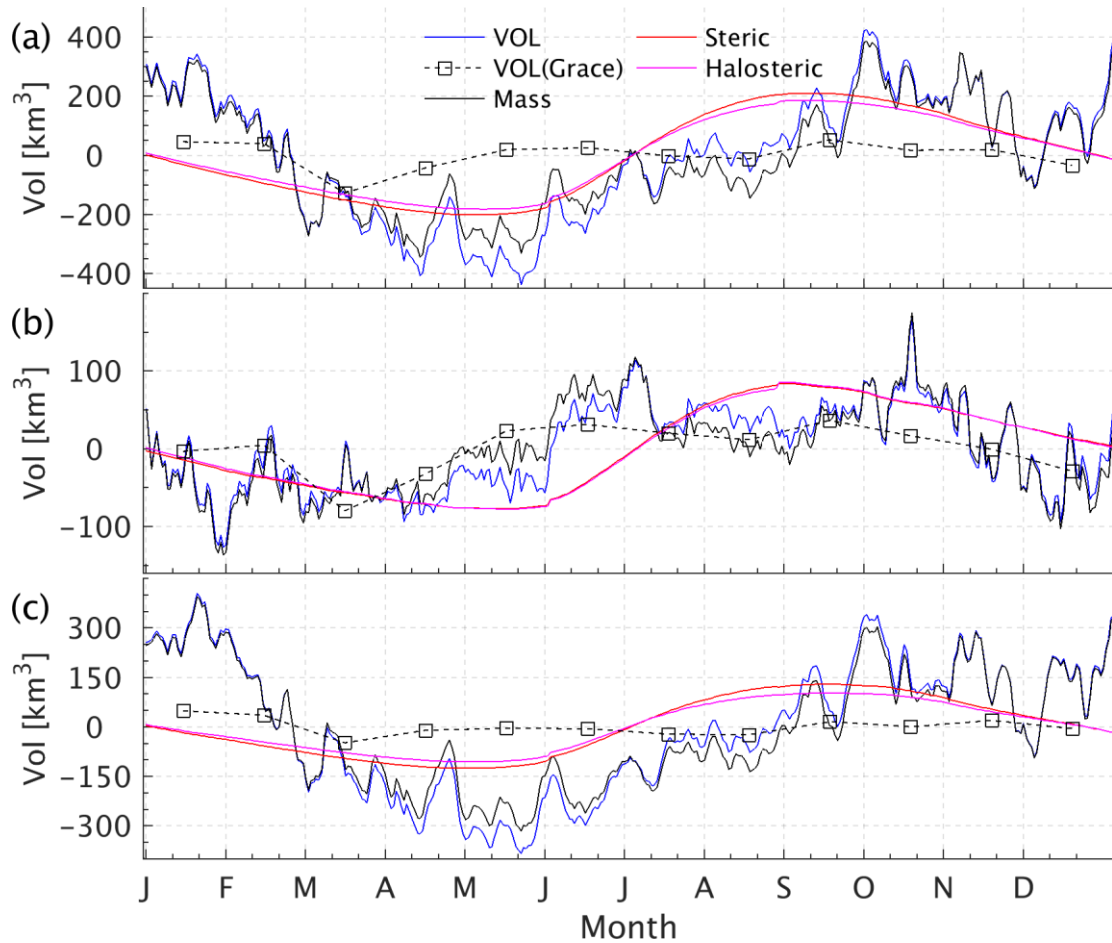
Figure 8. (a) Time series of total volume (VOL) anomaly in the Arctic Ocean (see Fig. 1 for the regions) and the contributions from mass changes (Mass) and steric effects (Steric). The halosteric component (Halosteric) and the GRACE-observed mass component are also shown. Panels (b) and (c) show the corresponding values in (b) the deep basin (>500 m) and (c) the shallow water (<500m).

Sea level changes reflect total volume changes. The Arctic volume anomalies, dominated by mass component, shows a clear seasonal cycle overlaid with sub-seasonal variability (Fig. 8a). Since the surface freshwater flux is treated as a virtual salt flux, river runoff and evaporation minus precipitation do not change the total volume directly. The seasonal volume variability, especially the mass component, is driven by volume exchanges with the Pacific and Atlantic Oceans. The steric component (red lines in Fig. 8), especially the halosteric component (magenta lines in Fig. 8), causes the volume to decrease in the winter season and increase in the summer season due to the sea ice formation/melting.

The model simulates more substantial seasonal mass variability than the GRACE measurement. Still, it fails to reproduce the secondary peak from May to July (Fig. 8a), which may relate to river discharge in the marginal seas. Splitting the total Arctic volume changes into contributions from the deep basin and coastal seas, we note that the secondary peak is related to volume changes in the deep basin from May to July (Fig. 8b) in both the model simulation and the GRACE observations. At the same time, volume anomalies are negative in the marginal seas. This antiphase of the volume anomalies in the deep basin and marginal seas seems to be driven by the cyclonic/anticyclonic wind pattern in the summer/winter season (Proshutinsky and Johnson, 1997).

Mean sea level anomalies from June to August (Fig. 9a) and from December to February (Fig. 9b) further reveal the antiphase of the sea level changes between the deep basin and the shallow waters. The mean pattern of wind stress anomalies (vectors in Fig. 9) indicates that wind-driven Ekman transport drives the water toward/away from the marginal seas, resulting in the antiphase of seasonal sea level variability in the deep basin and shallow waters.

The model simulation demonstrates the critical importance of exchanges with the Pacific and Atlantic Oceans for the Arctic volume changes at seasonal periods. The wind stress will further redistribute water in the Arctic Ocean, resulting in the antiphase pattern of sea level changes in the shallow waters and deep basins. Using a one-dimensional model, Peralta-Ferriz and Morison (2010) demonstrated that river runoff and evaporation minus precipitation (EmP) drive the basin-scale seasonal mass variation of the Arctic Ocean. This process is not included in our model simulations due to the virtual salt flux parameterization. But it should be noted that either input from river runoff and EmP (Peralta-Ferriz and Morison, 2010) or exchanges with the Pacific and Atlantic Oceans is large enough to drive the Arctic volume changes. Moreover, the wind stress will further redistribute the water to different regions. It is also expected that volume input from the rivers (~700 km^3) could significantly alleviate the negative volume anomalies from May to August in the marginal seas.
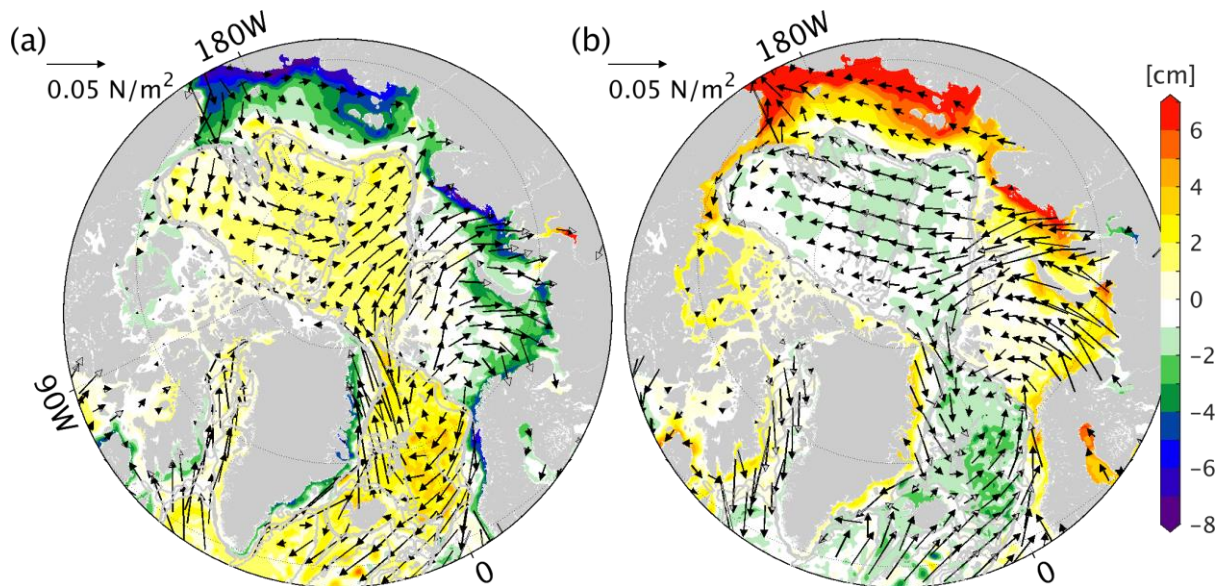
Figure 9. SLA (shading) and wind stress anomalies (vectors) to the climatology averaged from (a) June to August and (b) December to February. The daily output of ATLARC4km is used.

4.3 Decadal variability

The Arctic sea level shows significant decadal variability driven by cyclonic/anticyclonic wind patterns (Proshutinsky and Johnson, 1997), accompanied by freshwater content changes (Häkkinen and Proshutinsky, 2004;Köhl and Serra, 2014). Satellite altimetry observations were used to infer Arctic freshwater content increases (Armitage et al., 2016;Giles et al., 2012;Proshutinsky et al., 2019;Rose et al., 2019) and complement

305   freshwater content estimate using in-situ observations (Haine et al., 2015;Polyakov et al., 2020;Rabe et al.,

306   2014;Rabe et al., 2011). This section examines the spatial variability of Arctic decadal sea level and addresses

307   its relation to the mass, halosteric, and thermosteric components.

308   The ATLARC08km simulation revealed that the pronounced decadal sea level variability in the Canadian

309   and Eurasian Basins (Fig. 4c) is mainly due to the halosteric effect (Fig. 10b), with the mass components ac-

310   counting for 20-30%. The thermosteric effect dominates in the GIN seas, mainly relating to the convection pro-

311   cesses (Brakstad et al., 2019;Ronski and Budéus, 2005). Brakstad et al. (2019, see their Fig. A1) demonstrated

312   that a change from shallow convection to deep convection can lead to temperature changes of more than -0.2 °C

313   over the upper 600 m and salinity changes of 0.02 PSU over the upper 200 m, resulting in a significant thermo-

314   steric effect. In the north Atlantic Ocean, the thermosteric effect dominates. At the same time, the halosteric

315   effect compensates for the thermosteric effect in this region, rendering more considerable thermosteric height

316   variability than decadal total sea level variability.

317   Timeseries of sea level anomalies and their different components confirm that sea level variability is most-

318   ly halosteric in the Canadian (Fig. 10d, Armitage et al., 2016;Giles et al., 2012;Morison et al., 2012) and Eura-

319   sian basins (Fig. 10e) and that the thermosteric component contributes with a linear trend (not shown here). In

320   addition, the mass components contribute to the interannual sea level variability (blue lines in Fig. 10d and e) in

321   both the basins. We note that the mass changes are highly correlated in the Canadian and Eurasian basins

322   (r>0.98 with 95% significance level). They are positively correlated to the mass changes in the deep basin of the

323   GIN seas and the Arctic Ocean and are negatively correlated to mass changes in the Arctic marginal shelves,

324   especially in the East Siberian Sea, representing a barotropic response of sea level to changes of the intensity

325   and locations of the Icelandic low and the East Siberian high (e.g., Proshutinsky and Johnson, 1997). The halo-

326   steric component shows clearly decadal variability and is in phase with that in the Canadian Basin. The thermo-

327   steric component slightly compensates for the halosteric component.
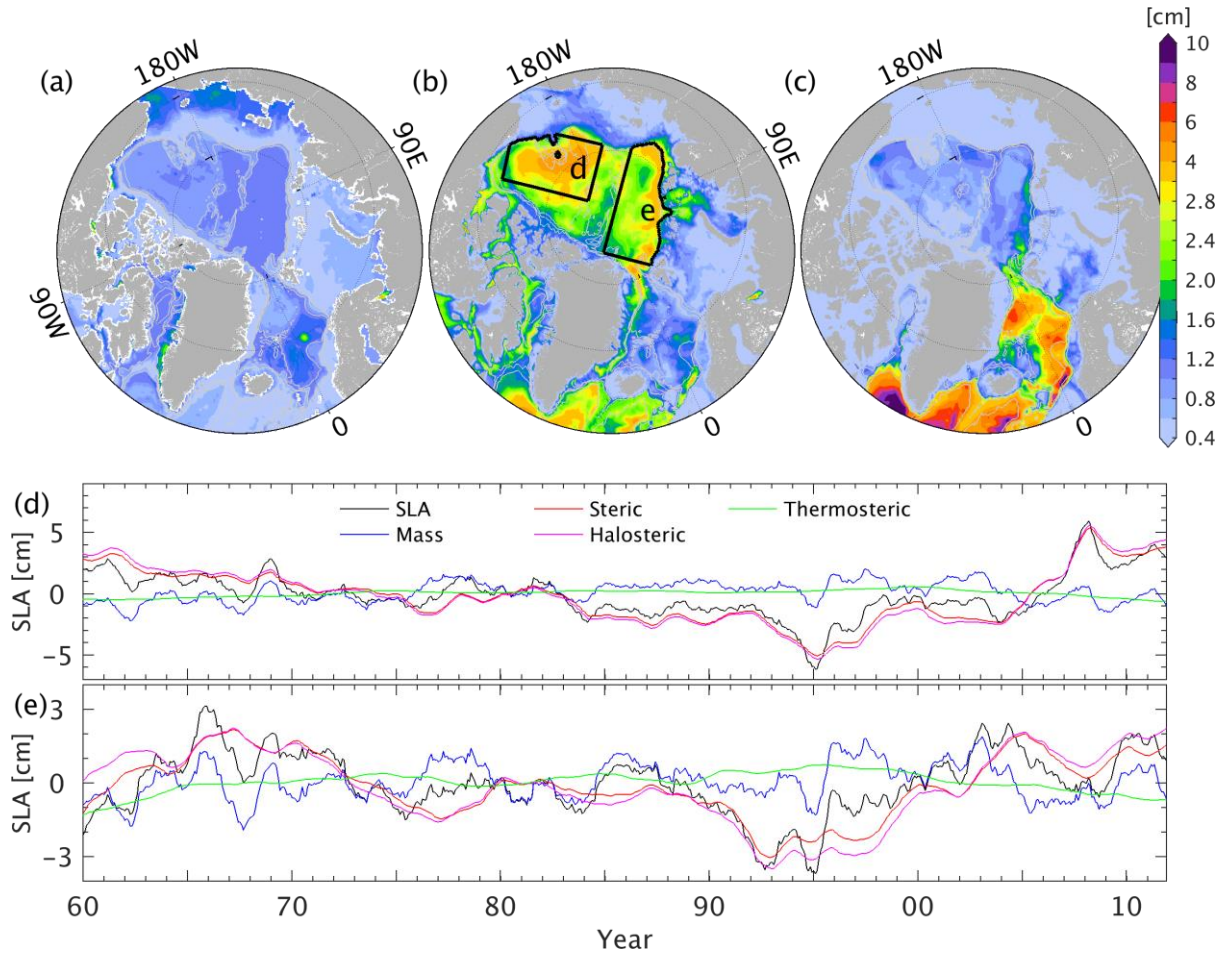
Figure 10. RMS variability at the decadal period of (a) bottom pressure anomaly, (b) the halosteric component, and (c) the thermosteric component. Panels (d) and (e) show the time series of sea level anomaly and mass, steric, and thermo/halosteric components in the Canadian and the Eurasian basins (see the regions in panel (b)), respectively. Linear trends in all the time series are removed in panels (d) and (e).

5 Capability of the observing system to monitor freshwater content variability

Observing Arctic freshwater content changes remains challenging (Proshutinsky et al., 2019). The results above and previous studies (Giles et al., 2012;Morison et al., 2012;Proshutinsky et al., 2019) have indicated that satellite altimetry could infer freshwater content changes. International efforts try to enhance the profiles observing system, including ice-tethered profilers (ITPs, Toole et al. (2016), doi:10.7289/v5mw2f7x), shipboard observations, and moorings. Here, we test their capability to monitor the freshwater changes in an idealized setting in which 1) we do not consider influences of observational errors and 2) we assume the profiles sample the top 800 m and the moorings sample from 65-800 m. Freshwater inventory is defined, as in Rabe et al. (2011) and Schauer and Losch (2019), as the freshwater fractions relative to a conventional reference salinity $S_0 = 34.8$ PSU integrated over depth, and freshwater content is the total freshwater inventory over a region:

$$FWC = \int FWI \, dA = \int \int_H^0 \frac{S_0 - S}{S_0} \, dz \, dA \tag{5}$$

with H being the depth of the 34.8 isohaline. The reference salinity indicates the mean salinity within the Arctic Ocean and can differ slightly in previous studies, which mainly impacts the mean state of freshwater content.

5.1 Satellite altimetry and GRACE measurements

Giles et al. (2012) used altimetric sea level observations, GRACE-based bottom pressure, and a static 1.5-layer model to infer freshwater changes in the Canadian Basin. They assumed that freshwater changes lead to sea level and isopycnal changes simultaneously, changing the water column's layer thickness and total mass. In this case, freshwater change in the water column is estimated as follows:

$$\Delta FW = \frac{S_2 - S_1}{S_2} \cdot \Delta h = \frac{S_2 - S_1}{S_2} \cdot \left(\eta' \cdot \left(1 + \frac{\rho_1}{\rho_2 - \rho_1} \right) - \frac{\Delta m}{\rho_2 - \rho_1} \right) \tag{6},$$

where $\rho_1 = 1025.0$ kg m^{-3} and $\rho_2 = 1028.0$ kg m^{-3} are the mean density in the top and bottom layers. $S_1 = 33.0$ PSU is the mean salinity in the top layer, and $S_2 = 34.8$ PSU is a reference salinity. η' and Δm are the sea level anomaly and bottom pressure anomalies observations. Morison et al. (2012) suggest that freshwater changes depend on steric height changes linearly and could be approximated by:

$$\Delta FW = \alpha \cdot \eta'_s \tag{7},$$

where α is an empirical constant estimated from in-situ profile observations and is set to 35.6 following Morison et al. (2012). The choice of α just contributes a static offset to freshwater content estimation in Eq. (7).

In the Canadian Basin, freshwater content changes and the two estimates show similar decadal variabilities, but differences remain in the seasonal and long-term trends (Figs. 11a and b). Since the halosteric effect dominates the steric effect, estimation using Eq. (7) matches the seasonal freshwater cycle well (red and black lines), considering the amplitude and phase. However, it overestimates the long-term trend (Fig. 11b) since Eq. (7) attributes the thermosteric effect to freshwater changes. Eq. (6) infers a much more substantial seasonal variability of freshwater content, and the phase does not always match the real freshwater content changes (blue and black lines).

368
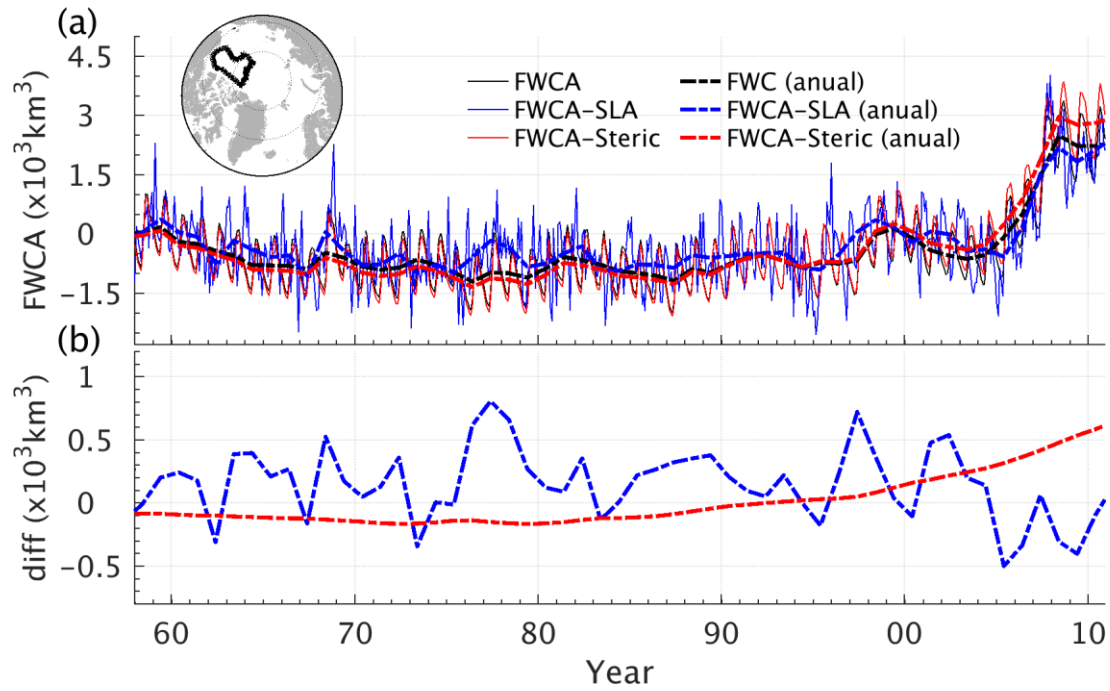
Figure 11. (a) Freshwater content anomalies (10^3 km^3) and approximated based on Eq. (6) in blue and Eq. (7) in red using the monthly output of ATLARC08km. The thick dashed lines are the annual mean values. (b) The differences of the approximated annual mean freshwater content anomalies based on Eq. (6) in blue and Eq. (7) in red to the annual mean freshwater content anomalies.

Eq. (6) assumes the upper layer adjusts simultaneously with sea level anomaly, which may not apply in the presence of baroclinic effects. To illustrate the limitation of Eq. (6), we take the differences between Feb. 2003 and Sep. 2002 (in which Eq. (6) fails to reproduce the phase and the amplitude of freshwater content changes) and between 2008-2010 and 1994-1996 (when Eq. (6) reproduces the freshwater changes well).

From Sep. 2002 to Feb. 2003 (Fig. 12a), anticyclonic wind stress anomalies occur in the Beaufort Sea, resulting in positive SLA through Ekman transport. However, freshwater content is reduced during this period. The salinity difference averaged over the central Arctic Ocean reveals that salinity increases in the top 30 m were caused by ice formation. At the same time, the isopycnal (27.9 kg m^{-3}) did not deepen (Fig. 12c) as predicted by Eq. (6). The assumption that freshwater content changes are captured by freshwater column thickness changes $\eta \cdot \left(1 + \frac{\rho_1}{\rho_2 - \rho_1}\right)$ (red dashed lines in Fig. 12c) fails to infer freshwater content changes in this case.

From 1994-1996 to 2008-2010, anticyclonic wind stress anomalies appeared in the Canadian Basin, accompanied by positive SLA and freshwater content anomalies (Fig. 12b). During that period, Ekman pumping deepens the isopycnals (blue and red lines in Fig. 12), accumulating more freshwater and reducing the local salinity over the top 300 m (Fig. 12d). In this scenario, the water column thickness change dominates the freshwater content variability, which is approximated by $\eta \cdot \left(1 + \frac{\rho_1}{\rho_2 - \rho_1}\right)$ (red dashed lines in Fig. 12d). Therefore, Eq. (6) captures the interannual freshwater content changes using satellite altimetric observations. Caution needs to be taken when inferring Arctic Ocean freshwater content changes using satellite altimetry observations and

390 GRACE measurements. In addition, Figs. 12b and 12d indicate that Eq. (6) can be only used in the Canadian

391 Basin where wind drives the sea level changes and the deepening/shoaling of the isopycnals.
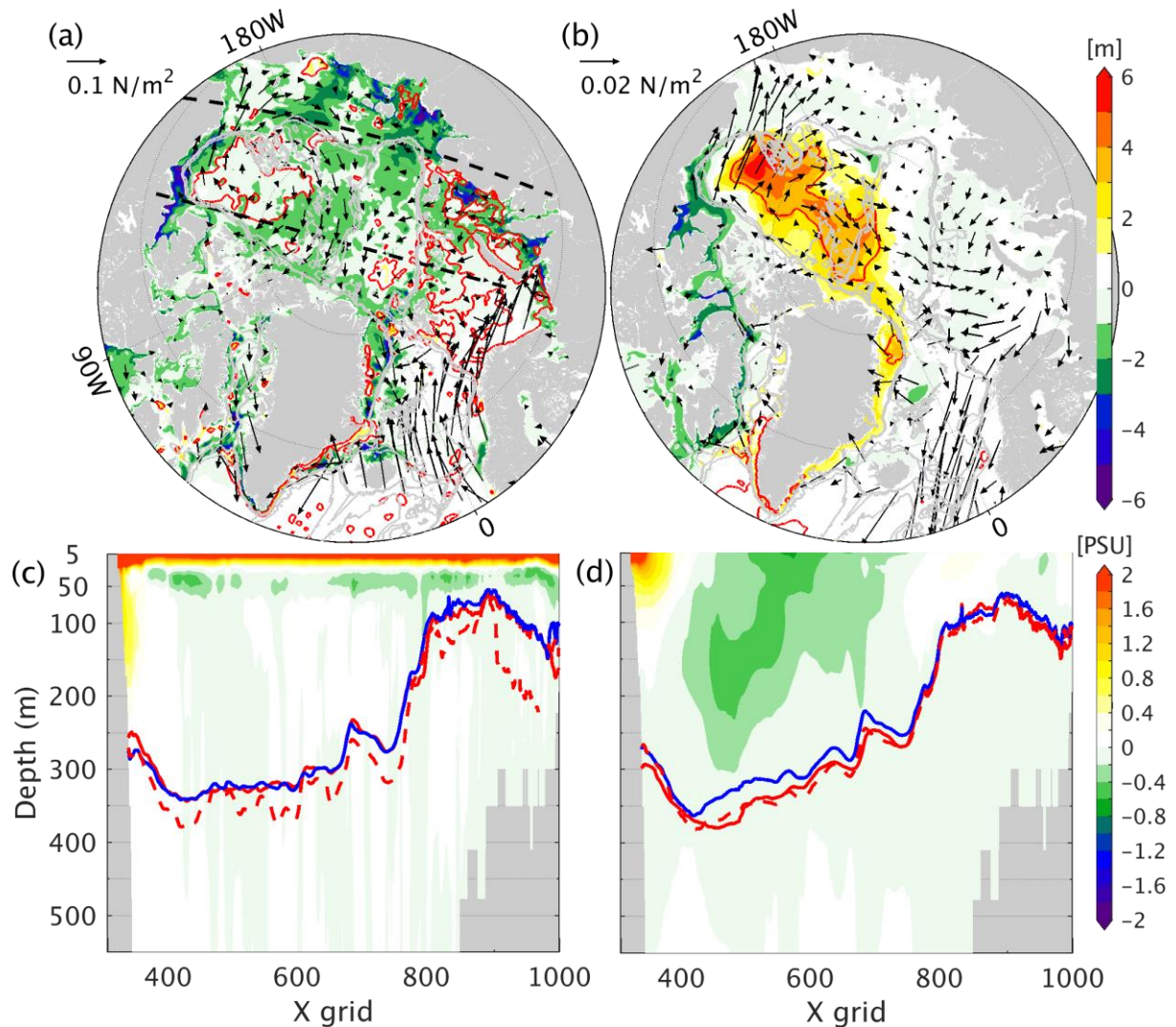
392 Figure 12. The differences of freshwater inventory in meters (shading), sea level anomaly (0.15 m contour,
393 black lines), and wind stress(vectors) between (a) Feb. 2003 and Sep. 2002, and (b) 2008-2010 and 1994-1996.
394 Panels (c) and (d) are the corresponding salinity differences (shading) average over the central Arctic Ocean
395 (black dashed lines in panel (a)). The blue lines denote the 27.9 kg m^{-3} isopycnal in Sep. 2002 and 1994-1996,
396 respectively. The red lines and red dashed lines are the 27.9 kg m^{-3} isopycnal and the diagnosed 27.9 kg m^{-3}
397 isopycnal with SLA and Eq. (5) in Feb. 2003 and 2008-2010, respectively.

398 5.2 In-situ profilers

399   In-situ profilers measure salinity directly, but they are limited by sea ice and distributed unevenly in time

400 and space. Over the past decades, the endeavor of polar expeditions and the evolving measurement techniques

401 (e.g., ITP) have generated a large number of hydrographic data in the central Arctic and subarctic seas (e.g.,

402 Behrendt et al., 2018). Using historical hydrographic observations and objective mapping techniques, previous

403 studies (e.g., Haine et al., 2015;Polyakov et al., 2008;Rabe et al., 2014;Rabe et al., 2011) have explored Arctic

404 freshwater content changes and the mechanisms on multi-year periods. However, the interpolated products suf-

405 fer from high uncertainties at timescales shorter than multi-year periods (e.g., Fig. 4 in the supplement of Rabe

406 et al., 2014), indicating observational gaps on resolving the seasonal to interannual freshwater content changes.
407 Besides, spatial observational gaps are observed (e.g., Fig. 7 in Rabe et al., 2011) but not explored yet. This
408 section examines how existing hydrographic observations could help reveal Arctic freshwater content changes
409 and identify observational gaps in time and space. Based on the spatiotemporal distribution of profiles compiled
410 by Behrendt et al. (2018) and an ensemble optimal interpolation (EnOI) scheme (Evensen, 2003;Lyu et al.,
411 2014), we test to what extent the generated synthetic profiles could help to reconstruct the "true" state (here the
412 ATLARC08km simulation) during the periods 1992 to 2012. Details of the EnOI scheme are given in Appendix
413 A.
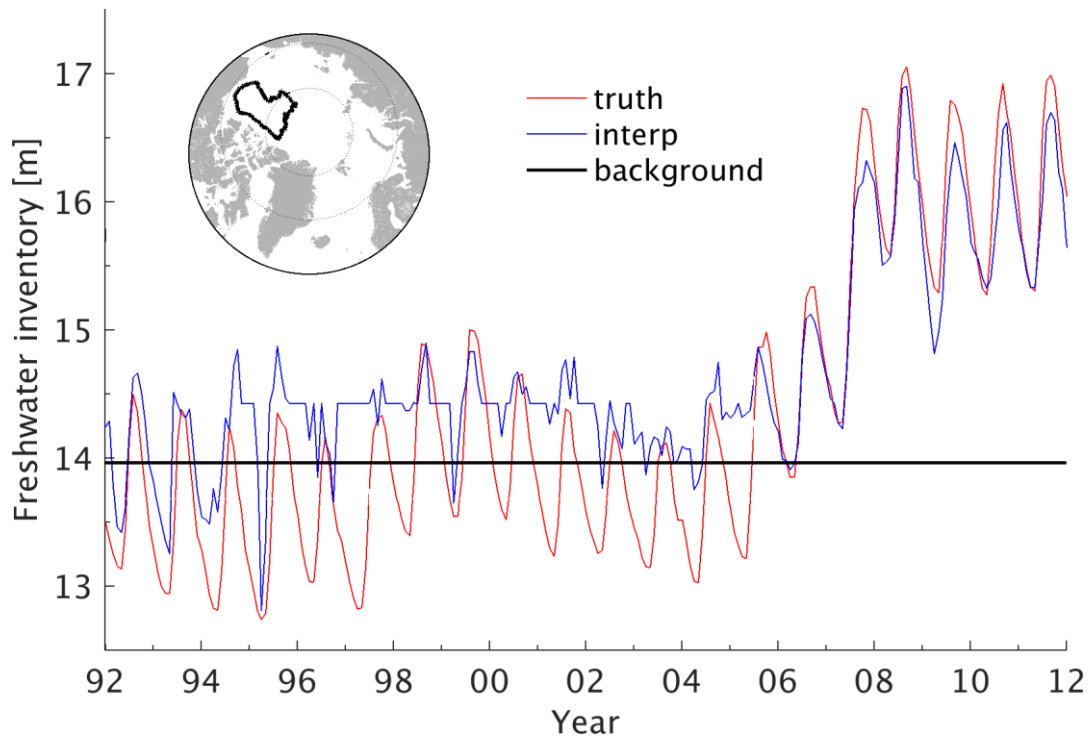
415 Figure 13. Mean freshwater inventory (in meter) in the Canadian Basin (enclosed by the black line in the top
416 subplot) from the background state, the "truth", and the optimal interpolation reconstructed state (see legend).

417 As shown in Fig. 13, the sparse in-situ profiles help bring the freshwater inventory in the background state
418 close to the "truth" state. However, it was not until 2007 that the reconstructed state reproduces the seasonal to
419 inter-annual freshwater inventory variability in the Canadian Basin, benefiting from the increasing number of
420 research activities and international collaborations. We further examined RMS errors of freshwater inventory
421 from 1992-2006 (Fig. 14a), 2007-2012 (Fig. 14b), and the corresponding profile locations (Fig. 14c and d). The
422 lack of in-situ profiles in the Arctic shelves (Figs. 14c and d) and in the deep basin from 1992-2006 (Fig. 14c)
423 results in pronounced errors. The ITP profiles (trajectories in Fig. 14d) enhanced the capability to observe the
424 Arctic freshwater changes in the deep basin and the winter season, significantly reducing freshwater inventory
425 uncertainties (Fig. 14b). Additionally, high errors remain in regions with high variability (e.g., EGC/WGC), in
426 the Laptev Sea and the Alaskan coast, extending from the coasts to the deep basin, underlining the observing
427 requirements.
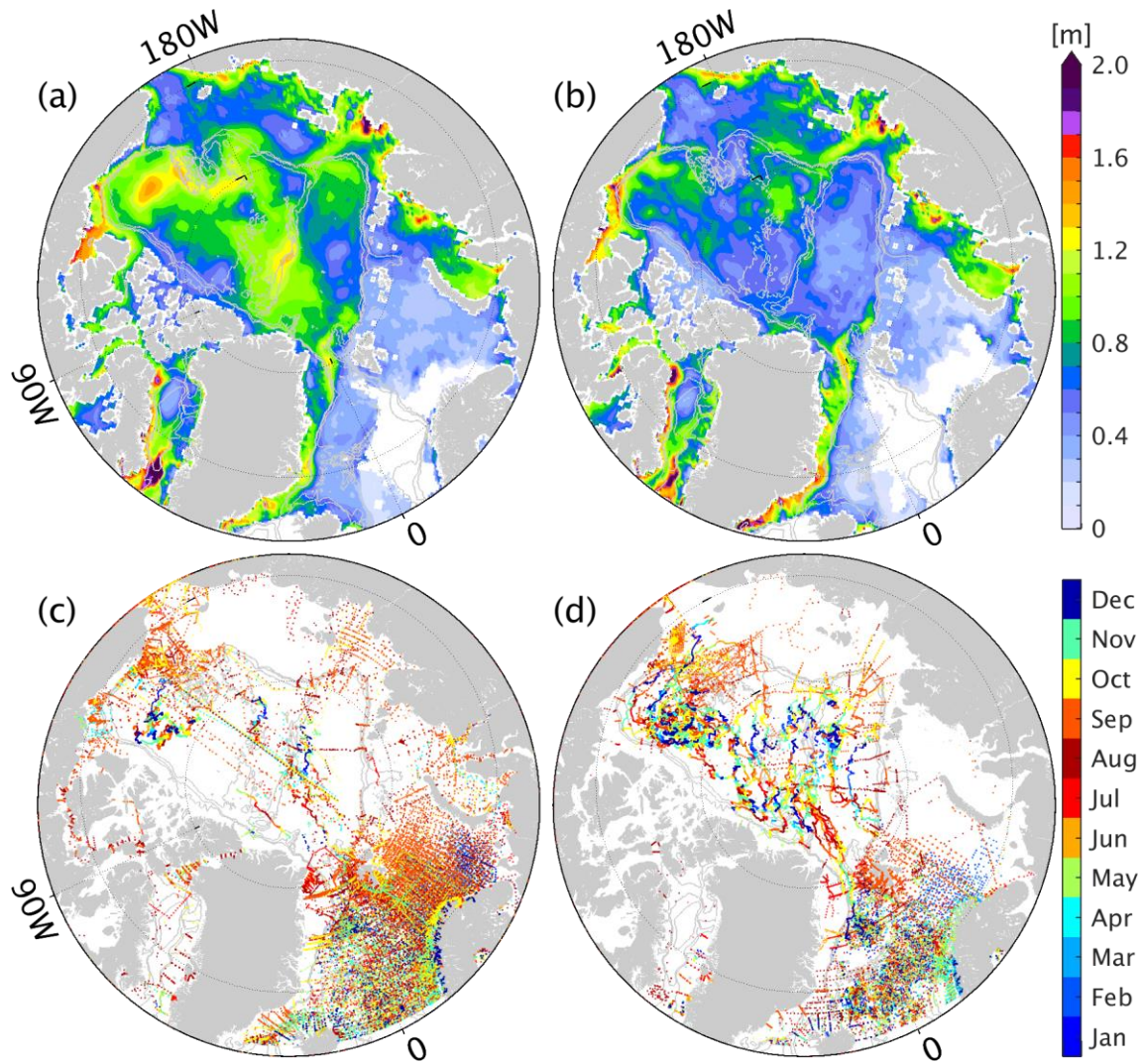
Figure 14. Root mean square errors of freshwater inventory (in meter) between the reconstructed state and the "truth" from (a) 1992-2006 and (b) 2007-2012. Panels (c) and (d) are the corresponding profile locations in different months (color bar).

The above results highlight that the increase of hydrographic observations has enhanced our ability to reconstruct the changes in Arctic freshwater content since 2007. A lack of hydrographic observations in the coastal areas results in significant errors in the marginal seas, which require extensive international collaborations.

6 Summary and conclusions

Sea level variability reflects changes in ocean dynamics, atmospheric forcing, and terrestrial runoff processes (Stammer et al., 2013). In particular, sea level observations have been applied to infer freshwater content changes (Armitage et al., 2016;Giles et al., 2012;Proshutinsky et al., 2019) in the central Arctic Ocean. To complement our understanding of the Arctic sea level variability and its mechanisms, we use two high-resolution ATLARC model simulations to investigate the Arctic sea level variability at different timescales and the relation with bottom pressure and thermo/halosteric effects, identifying critical observational gaps that need to be filled.

444   Both the model simulations and mooring observations reveal very high-frequency bottom pressure varia-
445   tions. The model simulations confirm that the bottom pressure anomaly is equivalent to sea level anomaly in
446   most areas of the Arctic Ocean at periods <30 days, reflecting the barotropic nature of this high-frequency vari-
447   ability. Correlation analyses show that the high-frequency sea level variability is caused by wind-driven Ekman
448   transport and propagations of these barotropic signals.

449   The seasonal sea level variability is dominated by volume exchanges with the Pacific and Atlantic Oceans
450   and the redistribution of the water by wind stress. Halosteric effects due to river runoff and ice melt-
451   ing/formation are also pronounced in the marginal seas and seasonal sea ice extent regions. Peralta-Ferriz and
452   Morison (2010) demonstrated that river runoff and EmP drive the seasonal cycle of the Arctic bottom pressure.
453   Although the virtual salt flux parameterization could not mimic the influences of volume input from rivers and
454   surface fluxes, the model simulations still simulate much stronger seasonal mass anomalies than the observa-
455   tions from GRACE. Either volume exchanges with the Pacific and Atlantic Oceans or volume input from river
456   runoff and EmP are large enough to cause the Arctic Ocean's seasonal volume variability. They should work
457   together, resulting in the Arctic seasonal volume variability. We speculate that using river runoff and EmP as
458   volume flux, rather than the virtual salt flux, could likely improve the volume and sea level variability in the
459   marginal seas from April to July since the volume inputs from river runoff could alleviate the negative volume
460   anomalies in the marginal seas caused by wind.

461   At decadal timescales, the model simulations further confirm that the pronounced sea level variability in the
462   central Arctic Ocean, especially in the Canadian Basin, is mainly a halosteric effect. Using the satellite altimet-
463   ric observations and GRACE observations, the method of Giles et al. (2012) could infer the freshwater content
464   changes in the Canadian Basin reasonably at timescales longer than one year since the upper layer (indicated by
465   the 27.9 kg m^{-3} isopycnal in this study) requires time to adjust to sea level changes. Inferring freshwater content
466   changes using a linear relation of freshwater content and steric height (Morison et al., 2012) reveals both the
467   interannual and the seasonal variability of freshwater content. However, caution needs to be taken since the
468   method attributes the thermosteric effects to halosteric effects, resulting in an additional linear trend. In addition,
469   uncertainties in the satellite altimetric and GRACE measurements make the estimation more complicated and
470   introduce significant uncertainties in the steric effects and freshwater content estimation (Ludwigsen and
471   Andersen, 2021).

472   The increasing number of international collaborations and new measurement techniques have generated a
473   large number of profiles. Previous studies have applied different objective mapping methods (Haine et al.,
474   2015;Polyakov et al., 2008;Rabe et al., 2014;Rabe et al., 2011) to reconstruct the Arctic freshwater content
475   changes and budget. However, the interpolated products still show high errors for the annual mean estimate of
476   freshwater content, indicating potential observational gaps in resolving the seasonal freshwater content cycle.
477   We further examined the observational gaps in time and space using monthly output from ATLARC08km.
478   Through reconstructing the salinity with synthetic observations, we note that the in-situ profile system seems to
479   capture the seasonal freshwater variability since the year 2007, encouraging further Arctic data synthesis studies
480   (Behrendt et al., 2018;Cheng and Zhu, 2016;Steele et al., 2001) with more complicated interpolation methods.
481   In addition, international collaborations need to be enhanced to fill in the observational gaps in the marginal seas.

482 Further observing system simulation experiments (e.g., Lyu et al., 2021;Nguyen et al., 2020) should be per-

483 formed in a coordinated fashion to develop an autonomous Arctic observing system (Lee et al., 2019;Sandu et

484 al., 2012) to meet the societal and scientific needs.

7 Data availability

486 The data used to create the plots in the paper are available at Pangaea

487 (https://doi.pangaea.de/10.1594/PANGAEA.912255). To access the results of the two high-resolution ATLARC

488 model simulations, please contact Dr. Nuno Serra at https://www.ifm.uni-

489 hamburg.de/en/institute/staff/serra.html. The Beaufort Gyre Exploration Program data were collected and made

490 available by the Woods Hole Oceanographic Institution (https://www2.whoi.edu/site/beaufortgyre/) in collabo-

491 ration with researchers from Fisheries and Oceans Canada at the Institute of Ocean Sciences and were derived

492 from https://www2.whoi.edu/site/beaufortgyre/data/mooring-data/. The North Pole Environmental Observatory

493 data were derived from http://psc.apl.washington.edu/northpole/Mooring.html. The satellite altimetric and

494 GRACE measurements were retrieved via http://www.cpom.ucl.ac.uk/dynamic_topography and

495 https://podaac.jpl.nasa.gov/announcements/2021-06-11-GRACE-and-GRACE-FO-L3-Monthly-Ocean-and-

496 Land-Mass-Anomaly-RL06-04-Dataset-Release. We gratefully acknowledge the Ice-Tethered-Profiler Pro-

497 gram based at the Woods Hole Oceanographic Institution (https://www.whoi.edu/itp) and the Unified Database

498 for Arctic and Subarctic Hydrography (https://doi.pangaea.de/10.1594/PANGAEA.872931) collected and com-

499 piled by the Alfred Wegener Institute.

500

501 *Author contribution.* G. Lyu performed the analysis and wrote the paper. N. Serra performed the model simula-

502 tions. D. Stammer proposed this study, and M. Zhou provided advice on the analysis.

503 *Competing interests.* The authors declare that they have no conflict of interest.

504

505 **Acknowledgments**

506   The authors wish to thank Benjamin Rabe and another anonymous reviewer for their valuable and helpful

507 comments on the manuscript. This work was supported partly through funding from project INTAROS, funded

508 by the European Union (Grant No. 727890). G. Lyu and M. Zhou also thank the support from project STRESS-

509 OR, funded by the National Natural Science Foundation of China (Grant No. 41861134040), and from the Ad-

510 vanced Polar Science Institute of Shanghai (APSIS). We thank ECMWF and NCEP for offering, respectively,

511 the ERAInterim and NCEP-RA1 atmospheric reanalysis data. We also thank NASA, BGEP, NPEO, and

512 NABOS for supplying observational data used in the model validation. All model simulations were performed

513 at the Deutsches Klimarechenzentrum (DKRZ), Hamburg, Germany. Contribution to the DFG funded Excel-

514 lence Cluster CLICCS at the Center für Erdsystemforschung und Nachhaltigkeit (CEN) of Universität Hamburg.

515 **Appendix A**

516 **An EnOI Scheme**

517   We use an EnOI scheme (Cheng and Zhu, 2016) to reconstruct the salinity in the Arctic Ocean using syn-

518 thetic observations. At one grid (denoted by subscript g), the analysis state φ_g^a is a linear combination of a back-

519 ground field φ_g^b and surrounding in-situ observations d:

520 $\varphi_g^a = \varphi_g^b + K(d - H\varphi_g^b) \cdot e^{-\frac{x^2}{2\sigma^2}}$ (A1),

521 where H is a transfer matric that maps model state from model space to observation points. In this study, the

522 background state of salinity φ_g^b is taken as the mean salinity at each grid over the period 1992-2012. K is the

523 Kalman gain, calculated as:

524 $K = \varphi_g' \varphi_g'^T H^T \left(H\varphi_g' \varphi_g'^T H^T + \gamma\gamma^T \right)^{-1}$ (A2).

525   The superscript T denotes matrix transposition. In this formulation, we use φ_g', the salinity deviation from

526 the mean salinity, to compute the error covariance of the background state ($\varphi_g' \varphi_g'^T$). We use monthly data from

527 the year 1992 to 2012 to compute φ', resulting in a total of 252 ensemble members. For simplicity, we assume

528 the representation errors γ only depend on depth, ranging from 0.09 PSU at the surface to 0.02 PSU in the deep

529 ocean, and are not correlated.

530   The use of ensemble members to approximate the background error covariance ($\varphi_g' \varphi_g'^T$) will inevitably

531 introduce long-distance correlations and propagate the observational information incorrectly over a much longer

532 distance. Therefore, we introduce a Gaussian function depending on the distance between observational

533 locations and the model grid (x in Eq. A1) and a decorrelation radius (σ in Eq. A1) to ensure that only

534 observations within the decorrelation radius σ of a model grid point could modify the analysis state.

535   Taking the "true" salinity state from August 1992 and observation locations from 2008 (black dots in Fig.

536 A1a), we test the impacts of the decorrelation radius on the analysis field. The background state is more saline

537 than the truth (Fig. A1a). With a 300 km decorrelation radius (Fig. A1b), the analysis state reduces the errors

538 near the observations while significant errors remain in regions far from observations. Increasing the

539   decorrelation radius to 1000 km, we see that salinity errors in the marginal seas, north pole areas, and the Baffin

540   bay are reduced (Fig. A1c). A 2400 km decorrelation radius further reduces salinity error in the Canadian Arctic

541   Archipelago (Fig. A1d). However, only slight improvements are observed in the central Arctic Ocean, and

542   errors in the Kara Sea are slightly increased. Since we focus on the Arctic freshwater content variability, we use

543   a 1000 km decorrelation radius throughout this study.

544
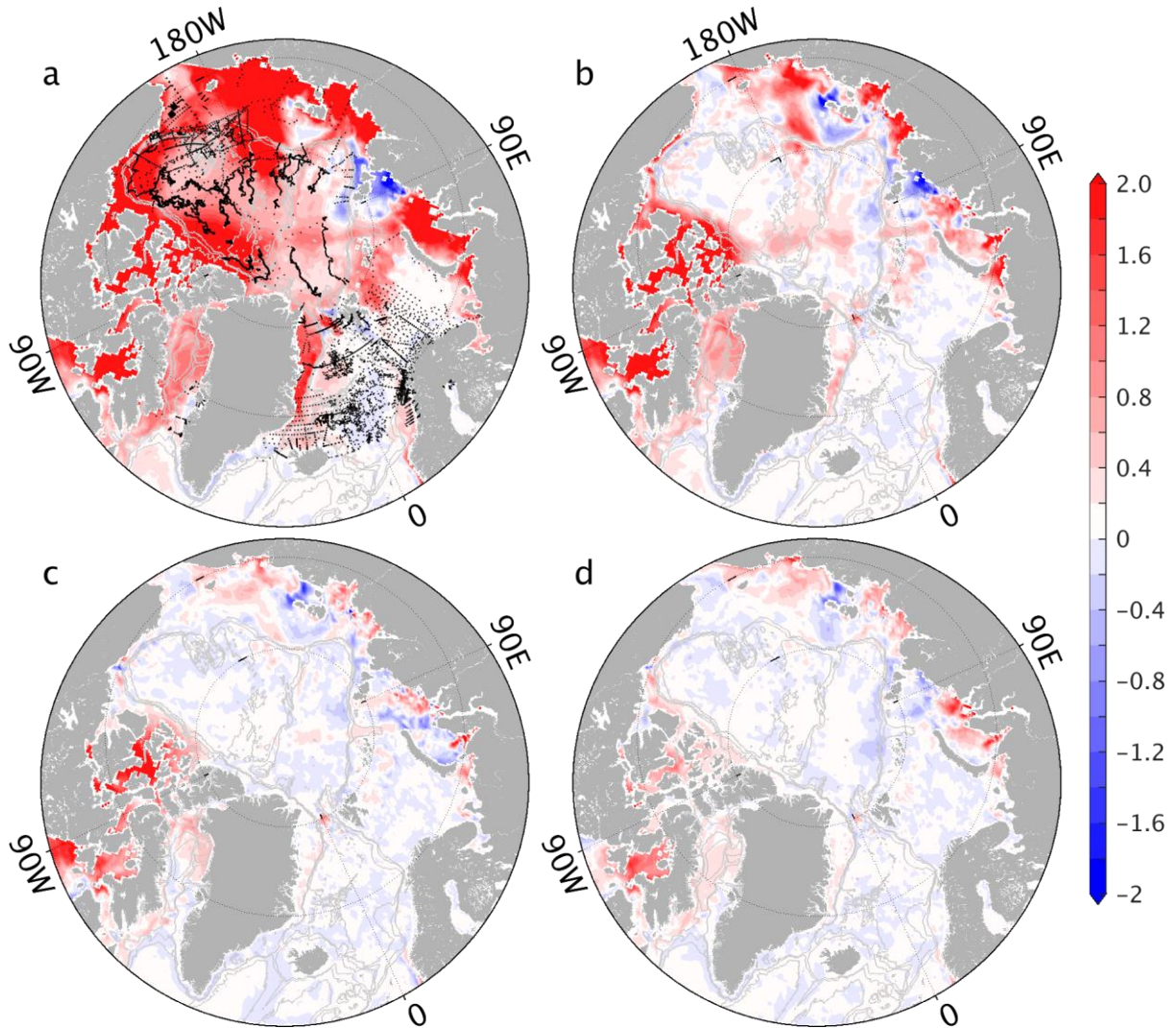
545

546   Figure A1. Example of sea surface salinity difference between (a) the background and the truth, (b) the analysis
547   with a decorrelation radius of 300 km and the truth, (c) the analysis with a decorrelation radius of 1000 km and
548   the truth, and (d) the analysis with a decorrelation radius of 2400 km and the "truth." Black dots in panel (a)
549   denote the locations of synthetic observations, sampled using sites of the observations from the year 2008.
550

551

References

AMAP, 2019. AMAP Climate Change Update 2019: An Update to Key Findings of Snow, Water, Ice and Permafrost in the Arctic (SWIPA) 2017. Arctic Monitoring and Assessment Programme (AMAP), Oslo, Norway. 12 pp.

Armitage, T. W., Bacon, S., Ridout, A. L., Thomas, S. F., Aksenov, Y., and Wingham, D. J.: Arctic sea surface height variability and change from satellite radar altimetry and grace, 2003–2014, Journal of Geophysical Research: Oceans, 121, 4303-4322, 10.1002/2015JC011579, 2016.

Behrendt, A., Sumata, H., Rabe, B., and Schauer, U.: Udash – unified database for arctic and subarctic hydrography, Earth Syst. Sci. Data, 10, 1119-1138, 10.5194/essd-10-1119-2018, 2018.

Boyer, T., Levitus, S., Garcia, H., Locarnini, R. A., Stephens, C., and Antonov, J.: Objective analyses of annual, seasonal, and monthly temperature and salinity for the world ocean on a 0.25 grid, International Journal of Climatology, 25, 931-945, 10.1002/joc.1173, 2005.

Brakstad, A., Våge, K., Håvik, L., and Moore, G. W. K.: Water mass transformation in the greenland sea during the period 1986–2016, Journal of Physical Oceanography, 49, 121-140, 10.1175/jpo-d-17-0273.1, 2019.

Calafat, F., Chambers, D., and Tsimplis, M.: Inter-annual to decadal sea-level variability in the coastal zones of the norwegian and siberian seas: The role of atmospheric forcing, Journal of Geophysical Research: Oceans, 118, 1287-1301, 10.1002/jgrc.20106, 2013.

Chambers, D. P., and Willis, J. K.: A global evaluation of ocean bottom pressure from grace, omct, and steric-corrected altimetry, Journal of Atmospheric and Oceanic Technology, 27, 1395-1402, 10.1175/2010jtecho738.1, 2010.

Chambers, D. P., and Bonin, J. A.: Evaluation of release-05 grace time-variable gravity coefficients over the ocean, Ocean Sci., 8, 859-868, 10.5194/os-8-859-2012, 2012.

Cheng, L., and Zhu, J.: Benefits of cmip5 multimodel ensemble in reconstructing historical ocean subsurface temperature variations, Journal of Climate, 29, 5393-5416, 10.1175/jcli-d-15-0730.1, 2016.

Dee, D. P., Uppala, S., Simmons, A., Berrisford, P., Poli, P., Kobayashi, S., Andrae, U., Balmaseda, M., Balsamo, G., and Bauer, d. P.: The era-interim reanalysis: Configuration and performance of the data assimilation system, Quarterly Journal of the royal meteorological society, 137, 553-597, 10.1002/qj.828, 2011.

Evensen, G.: The ensemble kalman filter: Theoretical formulation and practical implementation, Ocean Dynamics, 53, 343-367, 10.1007/s10236-003-0036-9, 2003.

Fekete, B. M., Vörösmarty, C. J., and Grabs, W.: High-resolution fields of global runoff combining observed river discharge and simulated water balances, Global Biogeochemical Cycles, 16, 15-11-15-10, https://doi.org/10.1029/1999GB001254, 2002.

Forget, G., Campin, J. M., Heimbach, P., Hill, C. N., Ponte, R. M., and Wunsch, C.: Ecco version 4: An integrated framework for non-linear inverse modeling and global ocean state estimation, Geoscientific Model Development, 8, 3071, 10.5194/gmd-8-3071-2015, 2015.

Fukumori, I., Raghunath, R., and Fu, L.-L.: Nature of global large-scale sea level variability in relation to atmospheric forcing: A modeling study, Journal of Geophysical Research: Oceans, 103, 5493-5512, 10.1029/97JC02907, 1998.

Giles, K. A., Laxon, S. W., Ridout, A. L., Wingham, D. J., and Bacon, S.: Western arctic ocean freshwater storage increased by wind-driven spin-up of the beaufort gyre, Nature Geoscience, 5, 194, 10.1038/ngeo1379, 2012.

Häkkinen, S., and Proshutinsky, A.: Freshwater content variability in the arctic ocean, Journal of Geophysical Research: Oceans, 109, 10.1029/2003JC001940, 2004.

Haine, T. W. N., Curry, B., Gerdes, R., Hansen, E., Karcher, M., Lee, C., Rudels, B., Spreen, G., de Steur, L., Stewart, K. D., and Woodgate, R.: Arctic freshwater export: Status, mechanisms, and prospects, Global and Planetary Change, 125, 13-35, https://doi.org/10.1016/j.gloplacha.2014.11.013, 2015.

Hibler, W. D.: A dynamic thermodynamic sea ice model, Journal of Physical Oceanography, 9, 815-846, 10.1175/1520-0485(1979)009<0815:adtsim>2.0.co;2, 1979.

Hibler, W. D.: Modeling a variable thickness sea ice cover, Monthly Weather Review, 108, 1943-1973, 10.1175/1520-0493(1980)108<1943:mavtsi>2.0.co;2, 1980.

Köhl, A., and Serra, N.: Causes of decadal changes of the freshwater content in the arctic ocean, Journal of Climate, 27, 3461-3475, 10.1175/jcli-d-13-00389.1, 2014.

Kalnay, E., Kanamitsu, M., Kistler, R., Collins, W., Deaven, D., Gandin, L., Iredell, M., Saha, S., White, G., and Woollen, J.: The ncep/ncar 40-year reanalysis project, Bulletin of the American meteorological Society, 77, 437-471, 10.1175/1520-0477(1996)077<0437:TNYRP>2.0.CO;2, 1996.

Koldunov, N. V., Serra, N., Köhl, A., Stammer, D., Henry, O., Cazenave, A., Prandi, P., Knudsen, P., Andersen, O. B., and Gao, Y.: Multimodel simulations of arctic ocean sea surface height variability in the period 1970–2009, Journal of Geophysical Research: Oceans, 119, 8936-8954, 10.1002/2014JC010170, 2014.

Lee, C. M., Starkweather, S., Eicken, H., Timmermans, M.-L., Wilkinson, J., Sandven, S., Dukhovskoy, D., Gerland, S., Grebmeier, J., Intrieri, J. M., Kang, S.-H., McCammon, M., Nguyen, A. T., Polyakov, I., Rabe, B., Sagen, H., Seeyave, S., Volkov, D., Beszczynska-Möller, A., Chafik, L., Dzieciuch, M., Goni, G., Hamre, T., King, A. L., Olsen, A., Raj, R. P., Rossby, T., Skagseth, Ø., Søiland, H., and Sørensen, K.: A framework for the development, design and implementation of a sustained arctic ocean observing system, Frontiers in Marine Science, 6, 10.3389/fmars.2019.00451, 2019.

Llovel, W., Willis, J. K., Landerer, F. W., and Fukumori, I.: Deep-ocean contribution to sea level and energy budget not detectable over the past decade, Nature Climate Change, 4, 1031-1035, 10.1038/nclimate2387, 2014.

Losch, M., Menemenlis, D., Campin, J.-M., Heimbach, P., and Hill, C.: On the formulation of sea-ice models. Part 1: Effects of different solver implementations and parameterizations, Ocean Modelling, 33, 129-144, 10.1016/j.ocemod.2009.12.008, 2010.

Ludwigsen, C. A., and Andersen, O. B.: Contributions to arctic sea level from 2003 to 2015, Advances in Space Research, 68, 703-710, 10.1016/j.asr.2019.12.027, 2021.

Lyu, G., Wang, H., Zhu, J., Wang, D., Xie, J., and Liu, G.: Assimilating the along-track sea level anomaly into the regional ocean modeling system using the ensemble optimal interpolation, Acta Oceanologica Sinica, 33, 72-82, 10.1007/s13131-014-0469-7, 2014.

Lyu, G., Koehl, A., Serra, N., and Stammer, D.: Assessing the current and future arctic ocean observing system with observing system simulating experiments, Quarterly Journal of the Royal Meteorological Society, n/a, 1-21, 10.1002/qj.4044, 2021.

Marshall, J., Adcroft, A., Hill, C., Perelman, L., and Heisey, C.: A finite-volume, incompressible navier stokes model for studies of the ocean on parallel computers, Journal of Geophysical Research: Oceans, 102, 5753-5766, 10.1029/96JC02775, 1997.

Morison, J., Kwok, R., Peralta-Ferriz, C., Alkire, M., Rigor, I., Andersen, R., and Steele, M.: Changing arctic ocean freshwater pathways, Nature, 481, 66, 10.1038/nature10705, 2012.

Nguyen, A. T., Heimbach, P., Garg, V. V., Ocaña, V., Lee, C., and Rainville, L.: Impact of synthetic arctic argo-type floats in a coupled ocean–sea ice state estimation framework, Journal of Atmospheric and Oceanic Technology, 37, 1477-1495, 10.1175/jtech-d-19-0159.1, 2020.

Nurser, A. J. G., and Bacon, S.: The rossby radius in the arctic ocean, Ocean Sci., 10, 967-975, 10.5194/os-10-967-2014, 2014.

Overland, J. E., Ballinger, T. J., Cohen, J., Francis, J. A., Hanna, E., Jaiser, R., Kim, B. M., Kim, S. J., Ukita, J., Vihma, T., Wang, M., and Zhang, X.: How do intermittency and simultaneous processes obfuscate the arctic influence on midlatitude winter extreme weather events?, Environmental Research Letters, 16, 043002, 10.1088/1748-9326/abdb5d, 2021.

Pawlowicz, R., Beardsley, B., and Lentz, S.: Classical tidal harmonic analysis including error estimates in matlab using t_tide, Computers & Geosciences, 28, 929-937, 10.1016/S0098-3004(02)00013-4, 2002.

Peralta-Ferriz, C., and Morison, J.: Understanding the annual cycle of the arctic ocean bottom pressure, Geophysical Research Letters, 37, 10.1029/2010gl042827, 2010.

Perovich, D., Meier, W., Tschudi, M., Hendricks, S., Petty, A., Divine, D., Farrell, S., Gerland, S., Haas, C., and Kaleschke, L.: Arctic report card 2020: Sea ice, 2020.

Polyakov, I. V., Alexeev, V. A., Belchansky, G. I., Dmitrenko, I. A., Ivanov, V. V., Kirillov, S. A., Korablev, A. A., Steele, M., Timokhov, L. A., and Yashayaev, I.: Arctic ocean freshwater changes over the past 100 years and their causes, Journal of Climate, 21, 364-384, 10.1175/2007jcli1748.1, 2008.

Polyakov, I. V., Pnyushkov, A. V., Alkire, M. B., Ashik, I. M., Baumann, T. M., Carmack, E. C., Goszczko, I., Guthrie, J., Ivanov, V. V., Kanzow, T., Krishfield, R., Kwok, R., Sundfjord, A., Morison, J., Rember, R., and Yulin, A.: Greater role for atlantic inflows on sea-ice loss in the eurasian basin of the arctic ocean, Science, 356, 285-291, 10.1126/science.aai8204, 2017.

Polyakov, I. V., Alkire, M. B., Bluhm, B. A., Brown, K. A., Carmack, E. C., Chierici, M., Danielson, S. L., Ellingsen, I., Ershova, E. A., Gårdfeldt, K., Ingvaldsen, R. B., Pnyushkov, A. V., Slagstad, D., and Wassmann, P.: Borealization of the arctic ocean in response to anomalous advection from sub-arctic seas, Frontiers in Marine Science, 7, 10.3389/fmars.2020.00491, 2020.

Ponte, R. M.: A preliminary model study of the large-scale seasonal cycle in bottom pressure over the global ocean, Journal of Geophysical Research: Oceans, 104, 1289-1300, 10.1029/1998JC900028, 1999.

Proshutinsky, A., Bourke, R., and McLaughlin, F.: The role of the beaufort gyre in arctic climate variability: Seasonal to decadal climate scales, Geophysical Research Letters, 29, 10.1029/2002GL015847, 2002.

Proshutinsky, A., Ashik, I., Häkkinen, S., Hunke, E., Krishfield, R., Maltrud, M., Maslowski, W., and Zhang, J.: Sea level variability in the arctic ocean from aomip models, J Geophys Res-Oceans, 112, 10.1029/2006jc003916, 2007.

Proshutinsky, A., Krishfield, R., Toole, J. M., Timmermans, M.-L., Williams, W., Zimmermann, S., Yamamoto-Kawai, M., Armitage, T. W. K., Dukhovskoy, D., Golubeva, E., Manucharyan, G. E., Platov, G., Watanabe, E., Kikuchi, T., Nishino, S., Itoh, M., Kang, S.-H., Cho, K.-H., Tateyama, K., and Zhao, J.: Analysis of the beaufort gyre freshwater content in 2003–2018, Journal of Geophysical Research: Oceans, 124, 9658-9689, 10.1029/2019jc015281, 2019.

Proshutinsky, A. Y., and Johnson, M. A.: Two circulation regimes of the wind-driven arctic ocean, Journal of Geophysical Research: Oceans, 102, 12493-12514, 10.1029/97JC00738, 1997.

Rabe, B., Karcher, M., Schauer, U., Toole, J. M., Krishfield, R. A., Pisarev, S., Kauker, F., Gerdes, R., and Kikuchi, T.: An assessment of arctic ocean freshwater content changes from the 1990s to the 2006–2008 period, Deep Sea Research Part I: Oceanographic Research Papers, 58, 173-185, https://doi.org/10.1016/j.dsr.2010.12.002, 2011.

Rabe, B., Karcher, M., Kauker, F., Schauer, U., Toole, J. M., Krishfield, R. A., Pisarev, S., Kikuchi, T., and Su, J.: Arctic ocean basin liquid freshwater storage trend 1992–2012, Geophysical Research Letters, 41, 961-968, https://doi.org/10.1002/2013GL058121, 2014.

Ronski, S., and Budéus, G.: Time series of winter convection in the greenland sea, Journal of Geophysical Research: Oceans, 110, https://doi.org/10.1029/2004JC002318, 2005.

Rose, S. K., Andersen, O. B., Passaro, M., Ludwigsen, C. A., and Schwatke, C.: Arctic ocean sea level record from the complete radar altimetry era: 1991–2018, Remote Sensing, 11, 1672, 10.3390/rs11141672, 2019.

Sandu, I., Massonnet, F., van Achter, G., Acosta Navarro, J. C., Arduini, G., Bauer, P., Blockley, E., Bormann, N., Chevallier, M., Day, J., Dahoui, M., Fichefet, T., Flocco, D., Jung, T., Hawkins, E., Laroche, S., Lawrence, H., Kristianssen, J., Moreno-Chamarro, E., Ortega, P., Poan, E., Ponsoni, L., and Randriamampianina, R.: The potential of numerical prediction systems to support the design of arctic observing systems: Insights from the applicate and yopp projects, Quarterly Journal of the Royal Meteorological Society, n/a, https://doi.org/10.1002/qj.4182, 2012.

Schauer, U., and Losch, M.: "Freshwater" in the ocean is not a useful parameter in climate research, Journal of Physical Oceanography, 49, 2309-2321, 10.1175/jpo-d-19-0102.1, 2019.

Smith, W. H. F., and Sandwell, D. T.: Global sea floor topography from satellite altimetry and ship depth soundings, Science, 277, 1956-1962, 10.1126/science.277.5334.1956, 1997.

Solomon, A., Heuzé, C., Rabe, B., Bacon, S., Bertino, L., Heimbach, P., Inoue, J., Iovino, D., Mottram, R., Zhang, X., Aksenov, Y., McAdam, R., Nguyen, A., Raj, R. P., and Tang, H.: Freshwater in the arctic ocean 2010–2019, Ocean Sci., 17, 1081-1102, 10.5194/os-17-1081-2021, 2021.

Stammer, D., Wunsch, C., and Ponte, R. M.: De-aliasing of global high frequency barotropic motions in altimeter observations, Geophysical Research Letters, 27, 1175-1178, 10.1029/1999gl011263, 2000.

700 Stammer, D., Cazenave, A., Ponte, R. M., and Tamisiea, M. E.: Causes for contemporary regional sea level
701 changes, Annual Review of Marine Science, 5, 21-46, 10.1146/annurev-marine-121211-172406, 2013.

702 Steele, M., Morley, R., and Ermold, W.: Phc: A global ocean hydrography with a high-quality arctic ocean,
703 Journal of Climate, 14, 2079-2087, 10.1175/1520-0442(2001)014<2079:pagohw>2.0.co;2, 2001.

704 Toole, J.M., Krishfield, R., Woods Hole Oceanographic Institution Ice-Tethered Profiler Program, Ice-Tethered
705 Profiler observations: Vertical profiles of temperature, salinity, oxygen, and ocean velocity from an Ice-
706 Tethered Profiler buoy system. NOAA National Centers for Environmental Information. Dataset.
707 https://doi.org/10.7289/v5mw2f7x, 2016.

708 Vinogradova, N. T., Ponte, R. M., and Stammer, D.: Relation between sea level and bottom pressure and the
709 vertical dependence of oceanic variability, Geophysical research letters, 34, 10.1029/2006GL028588, 2007.

710 Volkov, D. L., and Landerer, F. W.: Nonseasonal fluctuations of the arctic ocean mass observed by the grace
711 satellites, Journal of Geophysical Research: Oceans, 118, 6451-6460, 10.1002/2013jc009341, 2013.

712 Volkov, D. L., Landerer, F. W., and Kirillov, S. A.: The genesis of sea level variability in the barents sea,
713 Continental Shelf Research, 66, 92-104, 10.1016/j.csr.2013.07.007, 2013.

714 Woodgate, R. A., Weingartner, T. J., and Lindsay, R.: Observed increases in bering strait oceanic fluxes from
715 the pacific to the arctic from 2001 to 2011 and their impacts on the arctic ocean water column, Geophysical
716 Research Letters, 39, 10.1029/2012GL054092, 2012.

717 Zhang, J., and Rothrock, D. A.: Modeling arctic sea ice with an efficient plastic solution, Journal of Geophysical
718 Research: Oceans, 105, 3325-3338, 10.1029/1999JC900320, 2000.

719

720